Sensitivity Study of Physical Limits on Ground Motion at Yucca Mountain

Benchun Duan[1] and Steven M. Day[2]

[1] Department of Geology & Geophysics, Texas A&M University, College Station, Texas 77843

[2] Department of Geological Sciences, San Diego State University, San Diego, California 92182

Revised for Publication in *BSSA*

May 10, 2010

Abstract

Physical limits on ground motion parameters can be estimated from spontaneous-rupture earthquake models, but are subject to uncertainties in model parameters. We investigate physical limits at Yucca Mountain, Nevada, and assess sensitivities due to uncertainties in fault geometry, off-fault rock strength, the seismogenic depth, fault zone structure, and undrained poroelastic response of the fluid pressure. For the extreme scenario of nearly complete stress drop on the Solitario Canyon fault, peak ground velocity (PGV) at a site near the fault is sensitive to deep fault geometry and cohesive strength of shallow geologic units, while it is relatively insensitive to fault zone structure, the seismogenic depth, and pore pressure response. Taking previous estimates of Andrews et al. (2007) as a benchmark, a 10° reduction in dip (from 60˚ to 50˚) of the Solitario Canyon fault at depth, combined with doubled cohesion of shallow units, can increase both horizontal and vertical PGVs by over 1 m/s, to values exceeding 5 m/s. In a lower stress-drop scenario (constrained by regional extremes of co-seismic slip inferred from the paleoseismic record), PGV is most sensitive to fault geometry at depth, is only modestly affected by fault zone structure, and is insensitive to cohesion of shallow units and pore pressure response. Effects of rock strength on spectral acceleration are significant only at short periods (i.e., less than 3 s). The dipping normal-fault models predict asymmetric inelastic strain distributions with respect to the fault plane, with more intense inelastic deformation on the hanging wall, though that asymmetry may be moderated by poroelastic effects.

1. Introduction

Probabilistic seismic hazard analysis (PSHA) is usually undertaken assuming untruncated lognormal distributions for the ground motion parameters. A result is that when PSHA is applied at very low probability of exceedance levels (i.e., very long return times), as required, for example, for nuclear waste repositories, ground motion estimates are controlled by the upper tails of the distribution functions (e.g., Stepp et al., 2001). This procedure leads to extremely high ground-motion estimates that are widely considered to be unphysical. Thus, meaningful application of PSHA at very long return time requires that the standard methodology be supplemented with upper bound estimates for the relevant ground motion parameters (e.g., Bommer, 2002; Bommer et al., 2004).

The 1998 PSHA for Yucca Mountain, a potential high-level radioactive waste storage site, mostly in the context of a probability of exceedance of 10^{-4}/yr, is reported in Stepp et al. (2001). When it is extended to progressively lower mean-value hazard levels of 10^{-6}/yr, 10^{-7}/yr, and 10^{-8}/yr, the resulting peak ground velocity (PGV) are 3.5 m/sec, 7.0 m/sec. and 13.0 m/sec, respectively. These extremely large-amplitude ground motions at extremely low probabilities-of-exceedance, referred to as extreme ground motions (Hanks et al., 2006), are regarded as physically unrealizable and impose exceptional challenges to the design and construction of critical facilities at the Yucca Mountain site. To address these extreme ground motions, Hanks et al. (2006) recommend three areas of research, namely physical limits on ground motion, unexceeded values of ground motion, and event frequencies of occurrence. Unexceeded ground motions are those that have not happened for a specific time interval at a site, which may be constrained by precarious rocks for the past tens of thousands of years (e.g., Brune et al., 2003) and other geologic observations. On the other hand, physical limits on earthquake ground motion specify amplitudes of ground motion that cannot be exceeded for essentially open intervals of time at the site (Hanks et al., 2006), which may provide an important basis for upper bound estimates of ground motion at the site. Physical limits are unlikely to be established by statistical analysis of recorded ground motions (for example, as pointed out by Bommer et al., 2004, it is common to observe ground motion levels at least three standard deviations above the mean), and we have, instead, to be guided by consideration of the relevant physical processes that occur at the earthquake source and along the travel path of the seismic wave as it transits from the source to the site (Hanks et al., 2006).

Numerical modeling of the earthquake source and wave propagation provides a feasible means to study physical limits, by incorporating geological and geophysical observations. Commonly-used kinematic source models for ground motion calculations are not suitable for this purpose (Bommer et al., 2004), as these models ignore physical processes controlling earthquake rupture and the interactions between earthquake rupture and wave propagation. On the other hand, spontaneously dynamic rupture models, in which rupture propagation is determined by time-dependent stresses on the fault that can be coupled with off-fault processes, including possible material failure and wave reflections, can directly incorporate physical principles to examine physical limits on ground motion at a site. Two physical principles that can be applied to establish physical limits in general are (1) the maximum possible stress drop on the earthquake fault, and (2) the finite strength of the material through which seismic waves propagate. The former characterizes the maximum possible available energy at source to generate seismic waves, and the latter places a limit on the stress change in the medium through which seismic waves propagate to the site under investigation. We remark that in the context of physical limits on ground motion, we have to consider extreme, possible earthquake scenarios in which model parameters may be well beyond the reasonable range constrained by limited observations.

Physical limits on earthquake ground motion at the Yucca Mountain site have been studied by Andrews et al. (2007) (denoted as AN07, hereafter). They used a finite difference method and examined the two-dimensional, plane-strain, dynamic models of scenario earthquakes on the nearby faults. They found that the Solitario Canyon fault (SCF) is the one that can generate maximum ground motions at the site. Because there are no analytical solutions for spontaneous rupture problems with the requisite level of complexity, verification of numerical results from independent numerical methods is needed (e.g., Harris et al., 2009). Our first goal in this study is to verify calculations of ground motion at the site obtained by AN07. We use an explicit finite element (FE) method EQdyna (Duan and Oglesby, 2006, 2007; Duan and Day, 2008; Duan, 2008a, b) to revisit several of the solutions of AN07. The method is verified in our early work (Duan and Day, 2008) by obtaining very precise agreement with Andrews (2005)' independent finite difference solution to an elastoplastic rupture problem. We also compare our FE solutions at two different element sizes in this study to verify element-size-independence of our solutions (see Section 4). In elastoplastic calculations of this study, we simplify the bulk constitutive law used by AN07, reducing their hardening/softening variant of Mohr-Coulomb elastoplasticity to a constant-cohesion form. For models that yield similar surface slip, we find similar ground motion time histories at the site to those obtained by AN07, indicating that key solution features are robust with respect to minor model variations.

In a review of extreme ground motion estimation for the Yucca Mountain site, Hanks et al. (2006) recommended that additional simulations be undertaken to examine the sensitivity of the extreme estimates to assumptions such as stress state, faulting geometry, and material response. Our second goal in this study is to explore sensitivity of ground motion at the site to some of model uncertainties. The model and calculations of AN07 form the starting point. Templeton et al. (2009) have considered the effect on ground motion of possible activation of a shallow branch fault. Here we consider five additional factors: (1) time-dependent pore fluid pressure, (2) variations in the seismogenic depth, (3) changes in dip of the SCF at depth, (4) material strength parameters (i.e., cohesion and internal friction), and (5) a fault zone surrounding the fault with reduced seismic velocities.

Time-dependent changes in pore pressure have been shown to greatly reduce the dilational stepover distance that could be jumped by a propagating rupture (Harris and Day, 1993). Whether or not time-dependent pore pressure affects ground motion in general is an unresolved question. In AN07, pore pressure is assumed not to change during dynamic events and a static value of pore pressure before rupture is assumed. In this study, we will examine effects of time-dependent pore fluid pressure on ground motion at the site as a special case, with implications for general cases.

The seismogenic depth in the Basin and Range province may vary between 11 to 20 km (Stepp et al., 2001). The seismogenic depth may be defined as the maximum depth of shear stress drop in dynamic rupture models. By varying frictional properties on the fault, we can examine the effect of the seismogenic depth on ground motion.

Fault geometry at depth is generally poorly constrained by surface geology. A seismic reflection study of the area surrounding Yucca Mountain (Brocher et al., 1998) suggests that the dip of the SCF becomes shallower at depth. We will explore how possible changes in dip of the SCF at depth may affect ground motion at the site.

Material strength of the region is not well constrained by the limited available laboratory measurements. Thus, we examine sensitivity of ground motion at the site to the Mohr-Coulomb strength parameters. We start from the values of cohesion and internal friction for units proposed by AN07 and then change cohesion values to conduct this sensitivity test.

Low-velocity fault zones (LVFZs) have been detected by seismic investigations (both trapped wave and travel time analyses) along active faults, such as recent rupture zones of the 1992 Landers and 1999 Hector Mine earthquakes in the East California Shear Zone (e.g., Li et al.,1994, 2002) and the 1999 Izmit (Turkey) earthquake (e.g., Ben-Zion et al.,2003). This type of LVFZs may also exist around faults that have experienced healing of thousands years since the last earthquake, such as the Calico fault (Cochran et al., 2009). Effects of a LVFZ on dynamic rupture and near-field ground motion were examined by Harris and Day (1997) with assumption of elastic off-fault response, and more recently by Duan (2008a) with elastoplastic off-fault response. Without observations of the absence of a LVFZ along the SCF, we also examine sensitivity of ground motion at the site to a hypothetical LVFZ in this work.

2. Geological Structure, Fault Geometry, and Models

Yucca Mountain, Nevada, is the potential site of a repository for high-level radioactive waste. One safety issue is the potential for high levels of ground shaking from future earthquakes on nearby faults. Figure 1 shows surface traces of the faults near the site. Block-bounding normal faults have been active in this region since 13.25 m.y. before the present (Potter et al., 2004). Among these faults, the SCF has been identified as the one capable of generating maximum ground motion at the site (AN07). A dip of 60° for the SCF has been used by AN07. However, a shallower dip of the SCF at depth would be consistent with results from an active source seismic survey across the SCF, in which Brocher et al. (1998) interpreted a change in the fault dip at depth of ~ 1 km (see their Figure 13). The bottom part of their figure is reproduced here as Figure 2.

Figure 3 summarizes fault models and geologic structure we examine in this study. Color scales give the compressional wave velocity *Vp* in the models. Planar SCF, dipping west at an angle of 60°and having no fault zone, is the reference model A (denoted as PLWOFZ, hereafter) in this study, which is similar to that used by AN07. The geologic structure and the topography of the ground surface in PLWOFZ is adopted from AN07. To examine possible effects of a LVFZ, we add a 100-m wide fault zone with a reduction in seismic velocities of 20%, relative to wall rock of the same geologic unit, to the reference model A to generate the model B (denoted as PLWFZ). The fault zone is bisected by the fault. We remark that the choice of this 100-m wide LVFZ with 20% reduction in seismic velocities is very uncertain, but it may be a reasonable estimate for the SCF that is less active than the Calico fault in the Eastern California Shear Zone. A recent study shows seismic and geodetic evidence for a 1.5-km-wide LVFZ with

40%-50% reduction in seismic velocities along the Calico fault (Cochran et al., 2009). In the model C (denoted as KNWOFZ), the dip of the fault changes from 60° at shallow depth to 50° below -1 km depth, but fault zone is absent, based on a seismic reflection study by Brocher et al. (1998). In the model D (denoted as KNWFZ), both the change in dip at -1 km depth (the kink) and the fault zone are present. The plus sign represents the site at which we will examine ground motion in this study, which corresponds to the center of the repository shown as a rectangular box in Figure 3 of AN07. Because there is a large uncertainty in dip of the SCF at greater depth due to lack of constraints from either the reflection data (Brocher et al., 1998) or instrumental seismicity, we also examine another model (denoted as KN2WOFZ, not shown) with an additional change in dip of the SCF at -6 km depth (from 50° above to 40° below the depth), compared with KNWOFZ. Table 1 gives a brief description of these models.

A closer view of the model PLWFZ (Figure 3b) is shown in Figure 4. As in AN07, the geologic stratigraphy is offset on normal faults dipping to the west, and beds are tilted eastward between the faults. Notice that depth in this study is referred to the intersection of SCF and the ground surface, which is different from AN07 in which the reference of depth is the Yucca Crest. The positive direction of our vertical coordinate axis is upward. Thus, the water table in our study is at a uniform depth of ~ -490 m. Material properties outside the fault zone are adopted from AN07. When introducing a low-velocity fault zone, we keep the density and Poisson's ratio the same in each unit, but seismic velocities *Vp* and *Vs* are reduced by 20% and internal friction and cohesion may also decrease at depth. Material properties in PLWFZ, including density ρ, P and S wave velocities *Vp* and *V*s, Poisson's ratio ν, internal friction $tan\phi$, and cohesion *c*, are listed in Table 2.

3. Method

We use an explicit finite element dynamic code EQdyna (Duan and Oglesby, 2006, 2007; Duan and Day, 2008; Duan, 2008a, b) to simulate spontaneous rupture on the SCF and wave propagation in an inhomogeneous elastic or elastoplastic medium. The code has been verified in the SCEC/USGS dynamic code validation exercise (Harris et al., 2009).

The Mohr-coulomb plasticity has been implemented in the code (Duan and Day, 2008). The Mohr-Coulomb criterion states that when stress state at a point in a medium reaches a critical condition, the material point yields and plastic strain is generated at the point. We employ a 2D Cartesian coordinate system with x horizontal (positive east), y vertical (positive up), and the origin being at the surface outcrop of the SCF (see Figure 4). The critical condition in these 2D plane-strain models with relevant stress components σ_{xx}, σ_{yy}, and σ_{xy} is given as follows:

$$\begin{aligned} &\tau_{\max} \le \tau_{coulomb} \\ &\tau_{\max} = \sqrt{\sigma_{xy}^2 + ((\sigma_{xx} - \sigma_{yy})/2)^2} \\ &\tau_{coulomb} = c\cos\varphi + \sigma_m \sin\varphi \\ &\sigma_m = (\sigma_{xx} + \sigma_{yy})/2 \end{aligned} \quad , \qquad (1)$$

where c and φ are cohesion and internal friction angle of the material, respectively, and the sign convention of positive in compression is used. Before the criterion is violated, the material point behaves elastically. When the criterion is violated in a trial stress evaluation, the deviatoric stress components are adjusted by a common factor to meet the yield criterion (with no change in the mean stress σ_m, thus no inelastic volumetric strain). The plastic strain increments are calculated from the adjustments of the corresponding stress components. The accumulated plastic strain components ε_{xx}^{p}, ε_{yy}^{p}, and ε_{xy}^{p} are obtained by time integration of these increments, and the magnitude of plastic strain at the time step is given by

$$\varepsilon^{p} = \sqrt{(\varepsilon_{xy}^{p})^{2} + ((\varepsilon_{xx}^{p} - \varepsilon_{yy}^{p})/2)^{2}} \,. \qquad (2)$$

Duan and Day (2008) presented extensive tests of this numerical method, applied to elastoplastic rupture problems, including a comparison with an independent solution by Andrews (2005).

To assess the Mohr-Coulomb criterion in the medium, the absolute stress level throughout the entire model is required. In situ stress measurements can provide the stress state in the crust. Hydraulic-fracturing measurements in deep boreholes near Yucca Mountain (e.g., Stock et al., 1985) can be fit by a normal-faulting stress state that would be in neutral equilibrium (incipient stable sliding) with a coefficient of friction of 0.6±0.1 on a fault dipping 60°. We follow AN07 to choose a nominal coefficient of friction μ_0 of 0.55 to characterize the initial stress state in our dynamic models. We remark that μ_0 is not an actual frictional coefficient, but simply a parameter that characterizes the initial stress state on the fault. A procedure is needed to construct the initial stress field in the entire model that should be in static equilibrium. We adopt a two-step procedure in this study. In the first step, a first-order approximation of σ_{xx} and σ_{yy} is calculated while σ_{xy} is assumed to be zero. In the second step, a dynamic relaxation technique iteratively perturbs the first-order approximation to obtain an initial stress field that is in static equilibrium. In general cases where there are lateral variations in density (e.g., due to tilted layers in the above models) and topographic relief, the three components σ_{xx}, σ_{yy} and σ_{xy} in static equilibrium are all non-zero and depend on both x and y.

To obtain the first-order approximation of σ_{xx} and σ_{yy} for the first step, we approximate σ_{yy} by overburden and then approximate σ_{xx} by a factor R times σ_{yy} . R is chosen so that (provisionally taking σ_{xy} zero) a fault of dip θ would be in neutral equilibrium with a coefficient of friction of μ_0,

$$R = \frac{\sin(2\theta) - \mu_0[\cos(2\theta) + 1]}{\sin(2\theta) - \mu_0[\cos(2\theta) - 1]}. \quad (3)$$

The above discussion is valid in dry condition (e.g., above the water table). Below the water table, pore fluid pressure needs to be taken into account. In this case, the effective stress law applies. If p is pore fluid pressure, then σ_m in the Mohr-Coulomb criterion of equation (1) changes to

$$\sigma_m = (\sigma_{xx} + \sigma_{yy})/2 - p, \quad (4)$$

Notice p is a positive number, σ_m is reduced by pore fluid pressure, and rock becomes weaker when pore fluid pressure is present in the Mohr-Coulomb criterion. In the first step of the initial stress setup, R will be the ratio of effective stress as follows:

$$R = \bar{\sigma}_{xx} / \bar{\sigma}_{yy}, \bar{\sigma}_{xx} = \sigma_{xx} - p, \bar{\sigma}_{yy} = \sigma_{yy} - p. \quad (5)$$

Initial pore fluid pressure p_0 before an earthquake rupture can be considered in hydrostatic equilibrium and can be calculated by

$$p_0(y) = \rho_w g(y_w - y), \quad (6)$$

where, ρ_w and y_w are water density and water table depth, respectively, and $y<y_w$ (below the water table).

One approximation is to consider that pore fluid pressure p during a dynamic event does not change with time and always has a value of p_0. We denote this as the static pore pressure case. Since fluid diffusion distances will be negligibly small compared with all seismic wavelengths of interest, a more reasonable approximation is to use the undrained poroelastic response, in which case pore fluid pressure p responds to time-dependent changes in mean stress during a dynamic event. In this approximation (which we denote the time-dependent pore pressure case), changes in pore pressure $\Delta p(t)$ relative to p_0 are proportional to the time-dependent changes in mean stress, $\Delta\sigma_{kk}(t)/3$. For plane strain, with zero strain in the z direction,

$$\Delta p(t) = B\left(\frac{1+\upsilon}{3}\right)[\Delta\sigma_{xx}(t) + \Delta\sigma_{yy}(t)], \qquad (7)$$

where ν is the undrained Poisson ratio (Rice and Cleary, 1976), B is Skempton's coefficient and a value of 0.8 (e.g., Harris and Day, 1993) is chosen in this study. Equation 7 was previously employed in rupture simulations by Harris and Day (1993), who found that it led to significant effects--relative to the static pore pressure model--at fault stepovers, where large elastic changes in mean stress occur.

When we set up initial stress conditions, the R value (smaller than 1) from equation (3) is only applied from the free surface down to the nucleation depth, which is 10 km in this study. Below this depth, R is set to linearly increase to 1 (corresponding to zero shear stress) at bottom of the SCF, which is set to be 15 km in this study. This results in gradually decreasing shear stress toward the bottom of the fault, which is consistent with small slip at the bottom of a fault generally observed in kinematic inversions of large earthquakes (e.g., Oglesby et al., 2004). In all dynamic rupture simulations, we initiate rupture on the fault at the nucleation depth by assigning a fixed rupture speed (2000 m/s) within a nucleation patch with a half-length of Lc. A certain size of the nucleation patch, depending on the initial stress state and material properties, is required for rupture to be able to propagate spontaneously outside the patch. Spontaneous rupture is then governed by a linear slip-weakening friction law with a critical slip distance of D_0 in the form of

$$\mu(\delta) = \mu_s - (\mu_s - \mu_d)\min\{\delta, D_0\} / D_0, \qquad (8)$$

where δ, μ_s and μ_d are fault slip, static and dynamic friction coefficients, respectively. When shear stress reaches shear strength at a fault point, the frictional coefficient drops from μ_s to μ_d over the slip distance of D_0. The stress drop associated with this slip-weakening process drives the rupture to propagate spontaneously.

Quadrilateral elements are used throughout the entire model. Element size near the fault and the site is about 10 m (before shearing to conform the dipping fault geometry). Away from the fault and the site, element size increases at a small rate to move artificial model boundaries (i.e., all except for the free surface boundary at the top) far enough to prevent reflections from these boundaries from travelling back to the fault or the site during the duration of a calculation. If we take 8 element intervals (i.e., 9 nodes) per shear wavelength, the highest frequency in ground motion at the site accurately simulated in this study is about 20 Hz, given velocity values in Table 2.

For each model in this study, we conduct a pair of calculations: one assumes off-fault elastic response by changing the cohesion *c* in the Table 2 to a very high value to prevent plastic yielding from occurring, and the other uses Coulomb parameters in Table 2 to allow yielding. Given an initial stress field, we can adjust static and dynamic friction coefficients on the fault to obtain different rupture scenarios with different stress drops, rupture velocities, and final slips.

4. Comparisons with Previous Simulations

AN07 explored several rupture scenarios to estimate ground velocities under different conditions. Three main categories of scenarios are (1) the maximum possible surface slip of about 15 m, corresponding to nearly complete stress drop on the SCF (AN07), (2) the maximum paleoseismically-observed surface fault slip of 2.7 m for a single event on the SCF (Ramelli et al., 2004; AN07), and (3) the maximum paleoseismically-observed surface fault slip of 5 m for a single event in the Basin and Range Province (AN07). The first category may place physical limits on extreme ground motion at the site, and the third category gives estimates of maximum possible ground motion at the site consistent with geologic observations of past earthquakes in the region. Throughout this study, we simulate rupture scenarios similar to the first and the third categories of AN07. The first category always results in supershear rupture, while the third category permits both sub-Rayleigh and supershear ruptures. We switch between these two scenario categories by varying friction coefficients on the fault.

For calculations in the present section, our model differs from AN07 only in the small-scale details of the prestress and in our previously discussed formulation of the Mohr-Coulomb elastoplastic model, which we use without hardening/softening. Fault geometry and velocity structure of the model PLWOFZ are used in this section, as this model is closest to that used in AN07. Then in Section 5, we explore sensitivity of ground motion at the site to uncertainties in some of model parameters. When variations in these model parameters are introduced in Section 5, the final fault slip changes modestly, but for convenience we always refer to the scenarios in the high stress-drop category (the first category of AN07) as "15-m-slip" scenarios, and to those in the lower stress-drop category (the third category of AN07) as "5-m-slip" scenarios.

4.1. Maximum Possible Slip (~ 15 m) on Solitario Canyon Fault

Following AN07, we choose the static friction coefficient to be 0.7 in this set of simulations. The dynamic friction coefficient is chosen to be 0.1 at depth shallower than -12 km and to be 0.7 at greater depth to limit slip at the bottom of the SCF. Thus, stress drop above -12 km depth is nearly complete and rupture becomes supershear soon after it propagates outside the nucleation patch, which has a half length Lc of 130 m. D_0 is chosen to be a constant, at 0.25 m, to resolve the cohesive zone at the rupture tip (Day et al., 2005). These values of D_0 and Lc are used for all simulations of the 15-m-slip case in this study.

Figure 5 shows initial and final shear stresses, and final slip, on the modeled SCF from a pair of simulations with, respectively, elastic and elastoplastic off-fault response. The curves for elastic off-fault response can be compared with those in Figure 5 of AN07. The initial frictional strength and shear stress in our models are very similar to those in AN07. Differences in the initial stress include that (1) we do not have a constant shear stress patch near the nucleation depth, and (2) there are some bumps (or dips), particularly in the shear component, at layer boundaries in our initial stress. Our final shear stress curve is smoother than that of AN07. Final slip at shallow depth in our elastic calculation (~ 16 m) is a little larger than that of AN07 (~15 m). Final slip at the surface in our elastoplastic calculation is ~ 14 m. Time histories of the two velocity components at the site from elastic and elastoplastic calculations of our model are shown in left panels of Figure 6 and are directly compared with those of AN07 (their Figure 20), which are reproduced in right panels of Figure 6. Both waveforms and values of PGV from the two studies are very close to each other, particularly in the case with elastic off-fault response. Notice that we use constant cohesion in the elastoplastic calculation, while AN07 used varying cohesion with strain hardening/softening. The similarity in ground motion from the two studies suggests that in the 15-m-slip case, the site ground motion level is largely controlled by the strong P wave directivity, and is relatively insensitive to the details of the elastoplastic model and short-wavelength prestress variations.

4.2. Maximum Observed Surface Slip (~ 5 m) in the Basin and Range Province

Given the initial stresses in Figure 5, we explore different combinations of the static and dynamic friction coefficients to obtain ~ 5 m surface slip on the SCF. Here, final slip is determined by μ_d, while rupture speed is determined by both μ_d and μ_s. After a set of experiments, we find that $\mu_d = 0.37$ results in ~ 5 m surface slip (in the case with sub-Rayleigh rupture and off-fault elastic response). With this value of μ_d, we use $\mu_s = 0.9$ to obtain a sub-Rayleigh rupture, and $\mu_s = 0.7$ to obtain a supershear rupture. We choose $D_0 = 0.1$ m and Lc = 500 m in all simulations of the 5-m-slip case in this study. Compared with those in the 15-m-slip case above, the smaller value of D_0 can still well resolve the cohesive zone at the rupture tip, while the larger Lc is needed for rupture to propagate spontaneously outside the nucleation patch in these scenarios with a smaller stress drop.

Figure 7 shows stresses and final slip on the modeled SCF in this set of simulations. Calculations with elastic (E) and elastoplastic (P) off-fault response are each performed for both sub-Rayleigh (R) and supershear (S) ruptures. Initial shear stress is same for these calculations, while initial shear strength is different for sub-Rayleigh and supershear ruptures because of the difference in μ_s. Residual stresses due to plastic yielding result in some peaks and troughs in the final shear stress profile on the fault, particularly at layer boundaries. Final slip is reduced only near the free surface by plastic yielding in both the sub-Rayleigh and supershear ruptures. Time histories of ground velocities at the site from our calculations are shown in upper panels of Figure 8, and are compared with those from AN07 (their Figures 21 and 22) that are reproduced in lower panels of Figure 8. Results for both velocity time history and PGV agree closely between the two studies. The only obvious difference is in the horizontal PGV of the sub-Rayleigh rupture with off-fault plastic yielding, in which our PGV is about 17% higher than theirs. Their strain hardening/softening model results in more yielding than our constant cohesion model (Andrews, 2009, personal communication). Notice that in both the elastic and elastoplastic calculations, the horizontal PGV is larger in the sub-Rayleigh rupture than that in the supershear rupture, while the supershear rupture results in a larger vertical PGV than the sub-Rayleigh rupture. Given the cohesion and internal friction values in Table 2, which were also used by AN07, plastic yielding only occurs at shallow depth in all above elastoplastic models, including both 15-m-slip and 5-m-slip cases. Figure 9 shows plastic strain distributions from these calculations. It appears that plastic yielding occurs primarily above the Paleozoic dolomite unit (see Figure 4) as cohesion in this unit and below is 100 MPa in PLWOFZ, which is high enough to suppress plastic yielding. This feature in the plastic strain distribution results in reduced fault slip only near the free surface in these elastoplastic calculations, relative to corresponding elastic calculations, as shown in Figures 5 and 7. Larger stress drop in the 15-m-slip case generates more yielding, compared with the 5-m-slip case. Yielding occurs at the site in the 15-m-slip case only.

Finally, we have also verified that the solutions are essentially independent of element size. Figure 10 compares velocities and plastic strain distributions for the sub-Rayleigh, 5-m-slip case, for calculations done with 10 m elements (also used in all other calculations) and 25 m elements (similar to the 32 m finite difference cells used in AN07). We find no significant differences, apart from the minor effects of a little slower rupture (thus later wave arrivals at the site) with the coarse element size.

The similarity in both time histories of ground motion and PGVs from our study and AN07, despite some differences in the initial stress field and the details of the elastoplastic model, verifies ground motion calculations at the repository site obtained by AN07 by our independent numerical method.

5. Sensitivity of Ground Motion at the Site

In the above section of this study, physically-limited ground motion estimates are calculated from the spontaneous rupture models and compared with results from AN07 for verification of the numerical methods. However, uncertainties in physical processes and model parameters exist in these models. In this section, we examine how sensitive ground motion calculations are to these uncertainties. We start from how ground velocity at the site may be modified if pore fluid pressure changes according to equation 7 during dynamic events. Then we explore sensitivity of ground motions at the site to uncertainties in seismogenic depth, fault geometry at depth, material strength, and fault zone structure. We will work on the 15-m-slip case for supershear rupture, and on the 5-m-slip case for sub-Rayleigh rupture, as effects of these factors may be different for the two different rupture speeds. Calculations for elastic and elastoplastic off-fault response are performed for each case.

5.1. Time-dependent Pore Fluid Pressure

We work on the model PLWOFZ to examine time-dependent pore fluid pressure effects. Overall, time-dependent pore pressure has minor effect on ground motion at the site, relative to models with constant pore pressure. The effect is more visible in elastoplastic calculations (Figure 11) than in elastic calculations (not shown). In elastoplastic calculations, pore pressure affects both fault and off-fault material behavior (since both fault and material strength depend upon effective stress), whereas, in elastic calculations, pore pressure only affects fault strength, and therefore rupture propagation. As shown in Figure 12, time-dependent pore pressure results in larger fault slip than constant pore pressure, in both elastic and elastoplastic calculations. By Equation 7, time-dependent pore pressure responds to change in the mean stress. Upward rupture propagation causes compressional change in the mean stress within the footwall of the SCF, which in turn increases pore pressure and weakens rocks and results in more intensive plastic yielding (Figure 12). The resulting increase in plastic deformation on the footwall in both 15-m-slip and 5-m-slip cases reduces early-arrival peaks in horizontal waveforms. In both cases, larger fault slip at shallow depth results in visibly larger late-arrival peaks in horizontal waveforms.

In the subsequent simulations, we always use time-dependent pore pressure as we think that the undrained poroelastic response is a more reasonable approximation.

5.2. The Seismogenic Depth

In a dynamic model, the seismogenic depth may be defined as the maximum depth of shear stress drop on the fault. Shear stress drop on the fault is primarily controlled by initial stresses (including shear and normal stresses) and dynamic friction coefficient μ_d. As shown in Figures 5 and 7, shear stress decreases below the nucleation depth of -10.0 km (about 11.5 km down-dip distance). Furthermore, the dynamic friction coefficient μ_d is set to be equal to the static friction coefficient μ_s below a depth of -12.0 km (about 13.9 km down-dip distance) in the above models (and also other models except those in this subsection). As shown in Figures 5 and 7, the combination of the initial stresses and the frictional coefficients along the fault results in the maximum depth of shear stress drop (thus the seismogenic depth) of -12.0 km (13.9 down-dip distance) in the 15-m-slip case, and -11.1 km (12.8 down-dip distance) in the 5-m-slip case, respectively.

The seismogenic depth in the Basin and Range Province is in the range of 11 to 20 km below the surface (Stepp et al., 2001). To examine possible effects of a deeper seismogenic depth, we set μ_d as 0.1 in the 15-m-slip case and 0.37 in the 5-m-slip case along the fault up to a depth of -15 km (17.3 km down-dip distance for the dip of 60°). With the same initial stress profile along depth, this results in a deeper seismogenic depth in the 15-m-slip case while it does not change the seismogenic depth in the 5-m-slip case. Thus, we examine effects of a deeper seismogenic depth only in the 15-m-slip case. As shown in Figure 13, the seismogenic depth (the maximum depth of shear stress drop) in the new models of the 15-m-slip case is -13.5 km (15.6 km down-dip distance) and slip on fault is larger than that shown in Figure 12(b). This deeper seismogenic depth does not affect the early peaks in ground velocity at the site, but it does result in larger values of later peaks (Figure 14). In particular, the deeper seismogenic depth results in a larger PGV in horizontal ground velocity of the elastoplastic calculation as PGV is achieved in later peaks in this case (Figure 14).

5.3. Non-Planar Fault Geometry: Shallower Dip(s) at Depth

A large uncertainty exists in dip of the SCF at depth. As discussed in Section 2, a change in dip at shallow depth was imaged by a seismic reflection study (Brocher et al., 1998). Our model KNWOFZ, in which the dip of the SCF change from 60° above -1 km depth to 50° below it, is designed to capture this change in dip. At greater depth below several km, the dip is not constrained. We arbitrarily add an additional change in dip at -6 km depth (from 50° above to 40° below the depth) to KNWOFZ to construct the model KN2WOFZ. This allows us to examine trend of ground motion variations with a gradually shallower SCF in the down-dip direction. Ground velocity waveforms at the site from PLWOFZ, KNWOFZ, and KN2WOFZ are compared in Figures 15 and 16 for the 15-m-slip case and the 5-m-slip with sub-Rayleigh rupture case, respectively.

Comparing KNWOFZ with PLWOFZ, a shallower dip of SCF (KNWOFZ) at depth results in significantly larger PGV if off-fault response is elastic (left panels) in both 15-m-slip and 5-m-slip cases. Given the values of internal friction and cohesion for geologic units in Table 2, enhanced plastic yielding (Figure 17b) in KNWOFZ compared with that in PLWOFZ (Figure

12a) essentially cancels the effect of the shallower dip in the 15-m-slip elastoplastic calculation, while the effect (larger PGV) of the shallower dip in the 5-m-slip elastoplastic calculation remains substantial, probably because plastic yielding (Figure 17a) although increased compared with that in PLWOFZ (Figure 12c), is still much less extensive than in the 15-m-slip scenarios. In a later section, we will show that the effect of the shallower dip remains significant in 15-m-slip elastoplastic calculations when larger cohesions are assigned to units at shallow depth.

The larger PGV associated with the shallower dip at depth in KNWOFZ compared with that in PLWOFZ, observed in the elastic calculations of the two cases and the elastoplastic calculation of the 5-m-slip case, may be a combination of effects of larger fault slip and enhanced directivity. As shown in the 5-m-slip case with elastic off-fault response (Figure 17c), the down-dip ruptured length in KNWOFZ (with a shallower dip at depth) is longer than that in PLWOFZ, which results in ~ 30% larger fault slip along most part of the fault. Furthermore, a shallower dip of 50° below -1 km depth in KNWOFZ may enhance directivity effect because the site is closer to the forward rupture propagation direction (Somerville et al., 1997).

How ground motion at the site may change with a gradually shallower SCF along the down-dip direction can be examined by comparing ground motions obtained from KN2WOFZ and KNWOFZ. In the elastoplastic calculation of the 15-m-slip case (right panels of Figure 15), the waveform and PGVs are very similar between KN2WOFZ and KNWOFZ, primarily due to more extensive plastic yielding associated with shallower dip in this large stress-drop scenario. In the elastic calculation of the 15-m-slip case (left panels of Figure 15) and both elastic and elastoplastic (but with much less extensive yielding) calculations of the 5-m-slip case (Figure 16), earlier peaks in ground velocities from KN2WOFZ increase relative to those from KNWOFZ, probably because these peaks result from rupture on the fault at the vicinity of the site and peak slip velocity at the location is higher for shallower dips (given the same nucleation depth). While in these calculations, most of later peaks in ground motion stay at a similar level and the (largest) later peak in the horizontal component of the 5-m-slip case from KN2WOFZ even decreases relative to that from KNWOFZ (lower-left panel in Figure 16). This variation in later peaks in ground motion may be due to reduced directivity effect at the site in KN2WOFZ (i.e., the site being farther away from the forward rupture propagation direction due to a shallower SCF dip of 40° at depth) compared to that in KNWOFZ, though fault slip is larger in the former (Figure 17c).

By comparing ground motions from PLWOFZ, KNWOFZ, and KN2WOFZ, we might be able to shed light on the trend of PGV's variation at the repository site with possible gradually shallower dips along the down-dip direction of the SCF. If the strength of rock layers through which seismic waves transmit from the SCF to the site is relatively strong and thus the rock layers do not yield (i.e., in the elastic calculations) or yielding in these layers is not extensive (i.e., in the elastoplastic calculation of the 5-m-slip case), PGVs increase with shallower dips if they are achieved in earlier peaks of ground motion (i.e., the two components in the large stress-drop scenarios of the 15-m-slip case and the vertical components in the small stress-drop scenarios of the 5-m-slip case). If the rock layers are relatively strong and PGVs at the site are achieved in later peaks of ground motion (i.e., the horizontal component in the small stress-drop scenarios of the 5-m-slip case), PGVs increase when the dip changes from steep to moderate (e.g., from PLWOFZ to KNWOFZ) due to both large fault slip and enhanced directivity effect, while they may saturate or even decrease when the dip becomes very shallow at depth (e.g., from KNWOFZ to KN2WOFZ) due to reduced directivity effect at the site. If the rock layers are relatively weak (i.e., in the large stress-drop scenarios of the 15-m-slip case), enhanced yielding in the rock layers with shallower dips essentially prevents PGVs from increasing.

5.4. Variations in Cohesion

Although the values of the Mohr-Coulomb strength parameters (i.e., cohesion and internal friction) in Table 2, which are used in the elastoplastic calculations above and in AN07, may qualitatively characterize contrast in strength among different geologic units, the choice of these values is somewhat arbitrary, as noted in AN07. As shown in previous plastic strain plots, plastic yielding primarily occurs at shallow depth (i.e., above the Paleozoic Dolomite unit). In an attempt to see the effect of more yielding at greater depth, we reduce cohesion of wall rock in the Paleozoic Dolomite unit from 100 MPa to 25 MPa. In another experiment, we attempt to examine effects of less yielding at shallow depth by doubling cohesion of wall rock (denoted as DC, doubled cohesion) in Topopah Spring tuff, Calico Hill tuff, and Prow Pass tuff (cohesion being 20 MPa, 2 MPa, and 10 MPa for the three units, respectively, see Figure 4 for the depth ranges of these layers). Other parameter values do not change. We perform elastoplastic calculations with time-dependent pore pressure on models of PLWOFZ and KNWOFZ to test sensitivity of ground motion at the site to these variations in cohesion.

We find that although more yielding occurs within the Paleozoic Dolomite unit with the reduced cohesion in the 15-m-slip case (not shown), this smaller cohesion in the unit essentially has little effects on ground motions at the site (not shown), suggesting yielding near the site controls ground motion as yielding occurs near the site in the 15-m-slip case (Figures 12a and 17b). The reduced cohesion in the unit is still high enough to prohibit yielding at depth in the 5-

m-slip case and ground motions from SC (not shown) are the same as those with the original cohesion value.

Doubling cohesion values for the shallow units substantially increases PGVs at the site in the 15-m-slip case (Figure 18), in particular in the model of KNWOFZ (right panels in Figure 18), while its effect in the 5-m-slip case is relatively small (right panels in Figure 19). Thus, the previous result that there is little effect of shallower dips on the elastoplastic 15-m-slip case (right panels of Figure 15) no longer holds if there is substantially higher cohesion in the shallow units. Together with Figure 16 for the 5-m-slip case, this result suggests that PGVs at the site are very sensitive to fault geometry at depth, in the absence of any experimental data to rule out doubled cohesions in the shallow units. That is, uncertainties in deep fault geometry and material strength of shallow units are significant sources of uncertainty in estimates of physical limits on ground motion at the site.

The above effects of variations in cohesion on the ground motion at the site may be understood by comparing plastic strain distributions in Figure 19 (left panels) with those in Figure 17. In the test of DC, plastic yielding near the site in the 15-m-slip case is significantly reduced by higher cohesion, resulting in significantly higher PGVs (Figure 18). The effect of higher cohesion on PGVs is much less important in the 5-m-slip case (Figure 19), primarily because yielding does not occur near the site even with the original cohesion values (Figure 17a).

5.5. Low-Velocity Fault Zone

In this section, we compare ground motions at the site from PLWOFZ, PLWFZ, and KNWFZ to examine effects of a hypothetical 100-m wide LVFZ within which seismic velocities are reduced by 20% relative to wall rocks of the same unit. Figures 20 and 21 show ground motions at the site for the 15-m-slip case and the 5-m-slip case, respectively. When the LVFZ exists along the planar SCF (comparing PLWFZ with PLWOFZ), it has little effect on waveforms and PGVs in all calculations of the 15-m-slip case (Figure 20). In the 5-m-slip case (Figure 21), the LVFZ along the planar SCF reduces the earlier peaks in ground velocity at the site, while it tends to enhance later peaks in the elastic calculation. In particular, the vertical PGV in the elastoplastic calculation of the 5-m-slip (upper-right panel in Figure 21) is significantly reduced by the LVFZ. The above difference in the effect of the LVFZ on ground velocity at the site in the 15-m-slip and 5-m-slip cases may be related to difference in efficiency of seismic radiation to the site with the presence of the LVFZ. In the 15-m-slip case, rupture is supershear and seismic radiation to the site is very efficient, thus the LVFZ essentially has no effect. On the other hand, rupture is sub-Rayleigh in the 5-m-slip case and the LVFZ traps some seismic energy, resulting in a lower efficiency in seismic radiation to the site and reduced earlier peaks in ground velocity.

When both the 100-m wide LVFZ and the kink of the SCF at -1 km depth are present in the model KNWFZ, increase in PGV due to the shallower dip found above in Sec 5.3 only manifests in the horizontal component of the elastic calculation in the 15-m-slip case. Therefore, the PGV increases due to shallower dip that we saw in Sec 5.3 appear to be moderated by the presence of the LVFZ. In particular, in the 5-m-slip case (with sub-Rayleigh rupture), ground motion at the site is essentially dominated by the LVFZ effect, as evidenced by similarity in ground motion between PLWFZ and KNWFZ (Figure 21).

6. Discussion

In this section, we first summarize PGV and physical limit estimates from our simulations. Then we discuss application of our results to capping the ground motion at the repository site. Finally, we discuss more generally the inelastic strain distribution due to normal faulting within an inhomogeneous medium.

6.1. PGV at the Site and Physical Limits

Taking the work of AN07 as point of departure, we have explored the sensitivity of ground motion at the Yucca Mountain site to uncertainties in pore pressure behavior, the seismogenic depth, fault geometry (i.e., dip at depth), rock strength, and fault zone structure. Since our goal was to assess physical limits (as opposed to predicting likely ground motion levels), this exploration was done for scenarios that are extreme in two different senses--15-m-slip scenarios that represent near-total stress release, and 5-m-slip scenarios that represent maximum single-event observed surface slip in the Basin and Range Province. We found that, in large-slip scenarios, PGVs are sensitive to fault geometry at depth and cohesive strength of shallow units, while they are relatively insensitive to time-dependent pore pressure changes (represented through a non-zero Skempton poroelastic coefficient), the seismogenic depth, and fault zone structure.

Values of PGV from various simulations, as a function of surface fault slip, are summarized in Figure 22. Dashed lines in Fig 22 represent the envelopes of PGV estimates with off-fault yielding. With the cohesion values in Table2, a bounding PGV of about 4.78 m/s exists for near-total stress drop events (the 15-m-slip case), and the bounding PGV is about 3.48m/s for the events with reduced stress drop (the 5-m-slip case). The former are supershear rupture-velocity events (which here tend to maximize vertical PGV), while the latter set includes sub-Rayleigh rupture-velocity events (which tend to maximize horizontal PGV). With doubled cohesion values for shallow units (points labeled DC), the PGV bound for near-total stress drop events increases with surface slip (though with a slope much reduced relative to corresponding elastic calculations).

Corresponding results for spectral acceleration Sa (the pseudo-acceleration response spectrum) are shown in Fig 23. The effect of finite material strength is clearly period-dependent; the 3 s Sa limits are not reduced by plastic yielding (relative to the elastic estimates), nor are longer period values (not shown), whereas shorter-period Sa values are reduced by an amount that depends upon cohesive strength. Further refinement of these estimates for physical limits on ground motion parameters will depend, above all, upon better estimates of (or good upper bounds on) cohesive strength and internal friction angle of the geologic units.

AN07 also propose two additional factors that should be considered in attempting to use physical limits to bound extreme motion for this site. One is the possible reduction of P wave motion due to inelastic compaction of the Calico Hills tuff layer (which could potentially reduce the estimates). The second is allowance for even more extreme possibilities for dynamic stress drop than used in the current 15-m-slip scenarios, which AN07 suggest could increase the elastic estimates by up to a factor of 1.33. Whether or not this increase will be realized in the presence of Mohr-Coulomb strength limits depends on values of strength parameters, as shown by dashed lines in Figure 22.

6.2. Applications in Capping the Ground Motion at the Site

Physical limits provide one line of research for bounding ground motion extremes (and thereby establishing truncation levels for ground motion probability distributions) but the resulting bounds may not be very sharp, and should be weighed in the context of geological evidence as well. By definition, calculations to establish physical limits must explore rupture scenarios that are extreme relative to existing geological evidence (for per-event slip, rupture area, etc), and these scenarios should not be confused with likely events, or even geologically reasonable ones. For example, the 15-m-slip scenario considered here and by AN07, while necessary for quantifying the ground motion bounds attributable to limits on total stored strain energy, results in single-event slip that probably exceeds, by a substantial margin, any in the paleoseismic record for a crustal normal fault. AN07 propose the 5-m slip scenario as more representative of maximum single-event normal-fault slip in the Basin and Range Province, and a 2.7-m-slip scenario as representative of the maximum-slip event recognizable geologically for the SCF. Geologic evidence can also be incorporated by identifying evidence for the persistence of fragile geological features to estimate ground motion levels that have gone unexceeded for very long periods of time (Hanks, 2006). Upper-bound ground motion is inherently unobservable, and whatever bounds may ultimately be applied in practice will likely represent a judgment based on weighted consideration of multiple lines of evidence.

Uncertainties in dynamic model parameters are large due to limited observations, and thus sensitivity study is desirable. This study intends to explore effects of these uncertainties on physical limits of ground motion at the Yucca Mountain site. We explicitly explored uncertainties in pore-pressure behavior, the seismogenic depth, dip of deeper portion of the SCF, material strength in geologic units, and fault zone structure. We found that deeper fault geometry and shallow unit strength can have profound effects on PGV estimates at the site. Initial stress field was set up by taking into account what we know about stress state in crust in general and in situ stress measurements near the Yucca Mountain. Small-scale difference in the initial stress field between this study and AN07 does not affect PGV estimates at shown in Section 4. Frictional laws and parameters for natural faults are not well constrained. However, similarity in both waveforms and PGVs between this study and AN07 shown in Section 4 suggests that ground motion at the site is insensitive to details of frictional laws and their parameters. For example, AN07 used a time-weakening friction law with a constant time interval for friction to drop, which results in an equivalent slip-weakening law with variable critical slip distances D_0 in calculations with elastic off-fault response. As discussed in Section 3, we use a slip-weakening law with a constant critical slip distance D_0 in this study. Furthermore, we choose values of D_0 as small as possible in each case to maximize short-period ground motion, as long as these values can well resolve the cohesive zone at the rupture front to ensure numerical accuracy in dynamic models. This results in different values of D_0 used in the 15-m-slip and 5-m-slip cases. In short, we believe that dynamic rupture models are a powerful tool to study physical limits on ground motion even with large uncertainties in model parameters.

Finally, we remark that models in this study (also in AN07) are two dimensional in plane-strain geometry, which corresponds to constant east-west cross sections and assumes that fault slip extends indefinitely in the north-south direction. For this 2D geometry, the moment (thus the magnitude) of an earthquake event is not defined. It is expected that PGVs in these 2D models will be generally larger than those from equivalent 3D models, if focusing effects from wave propagation in 3D do not affect PGVs at the site.

6.3. Inelastic Strain Distribution Generated by Normal Faulting

An asymmetric (relative to the fault plane) inelastic strain distribution is generated by normal faulting on the dipping SCF in calculations with constant pore pressure during dynamic events, as shown in Figure 9 (a) and (b). A first-order feature in asymmetry of inelastic strain distribution is that inelastic strain is larger and is distributed over a wider zone on the hanging wall than it is on the footwall. Another first-order feature is that the zone of inelastic strain is very narrow (even absent) at great depth and becomes wider at shallower depth. This latter feature may result in "flower-like" fault damage zone (taking inelastic deformation as a proxy for rock damage), as suggested by a recent calculation (Ma, 2009) for a homogeneous medium.

Greater inelastic deformation on the hanging wall side would be expected simply because, in up-dip propagation of normal faulting, the medium is in extension (and therefore has a lower Mohr-Coulomb shear limit) near the rupture front on the hanging wall side. However, there are some complicated factors. The first factor is pore fluid pressure. As shown in Figure 12(a), when pore fluid pressure is time dependent during a dynamic event, more intense inelastic strain occurs on the footwall side (in the Prow Pass tuff unit in this case). This is caused by increase of pore fluid pressure in the footwall and decrease of pore fluid pressure on the hanging wall when rupture propagates upward from depth (since an increase in pore pressure weakens a Mohr-Coulomb material, while a decrease strengthens it). The second factor may be rupture velocity. In the 5-m-slip case, most sub-Rayleigh ruptures do not generate obvious asymmetry in plastic strain, as shown in Figures 9(c), and 12(c). A third factor is the dip of the normal fault. It appears that the asymmetry (greater deformation on the hanging wall side) is enhanced by a shallower dip below -1 km depth, as seen by comparing Figures 17 and 12. The significance of this purely geometrical effect of fault dip in enhancing inelastic strain on the hanging wall side is also suggested by the work of Ma (2009), who found higher inelastic strain on the hanging wall side in simulations of thrust faulting, despite the fact that in that case the principal rupture-front extension is expected to be on the footwall side.

7. Conclusions

Taking the work of AN07 as a point of departure, we investigated physical limits on ground motion at the Yucca Mountain site using numerical simulations of SCF scenario earthquakes. We have verified the reliability of the numerical simulations by (i) demonstrating close agreement with previous solutions obtained with an independent (finite difference) method by AN07 and (ii) showing that our own (finite element) solutions are element-size independent to high precision. In the subsequent sensitivity study, we find that, in the most extreme (15-m-slip) stress-drop models, PGV is sensitive both to dip of the deep portion of the SCF and to cohesive strength of shallow geologic units. In these most extreme models, PGV is relatively insensitive to the seismogenic depth, to fault-zone elastoplastic parameters, to the cohesive strength of the deep units, and to poroelastic fluctuations in fluid pressure. For the less extreme (5-m-slip) stress-drop models, the PGV bound remains sensitive to fault dip, but is no longer sensitive to shallow-unit cohesion values. The corresponding effect of cohesive strength on extremes of spectral acceleration is period dependent, cohesion uncertainties having little importance at periods of 3 s and longer. Improved estimates of the ground motion parameter bounds summarized in Figures 22 and 23 will depend upon establishing better upper bounds on the strength parameters of the shallow geologic units, and perhaps (if those strength bounds turn out to be significantly higher than values in Table 2) on the deep fault geometry of the SCF.

Data and Resources. All data used in this paper came from published sources listed in the references.

Acknowledgements. We are grateful to D. J. Andrews for helping us with the comparison of numerical results and for helpful discussions and encouragement. We thank Associate Editor Dr. A. McGarr and two anonymous reviewers for their helpful comments that improve this manuscript. This research was supported by the Southern California Earthquake Center through a grant from the U.S. Department of Energy/Pacific Gas and Electric Extreme Ground Motions project. SCEC is funded by NSF Cooperative Agreement EAR-0529922 and USGS Cooperative Agreement 07HQAG0008. The SCEC contribution number for this paper is 1325.

References

Andrews, D. J., Thomas C. Hanks, and John W. Whitney (2007). Physical limits on ground motion at Yucca Mountain, *Bull. Seismol. Soc. Am.*, 97, 1771-1792, doi:10.1785/0120070014.

Bommer, J. (2002). Deterministic vs. probabilistic seismic hazard assessment: an exaggerated and obstructive dichotomy, Journal of Earthquake Engineering, Vol. 6, Special Issue 1, 43-73.

Bommer, J. J., N. A. Abrahamson, F. O. Strasser, A. Pecher, P.-Y. Bard, H. Bungum, F. Cotton, D. Fah, F. Sabetta, F. Scherbaum, and J. Studer (2004). The challenge of defining upper bounds on earthquake ground motions, *Seism. Res. Lett*. 75, 82-95.

Brocher, T. M., W. C. Hunter, and V. E. Langenheim (1998). Implications of seismic reflection and potential field geophysical data on the structural framework of the Yucca Mountain-Crater Flat region, Nevada, *Geol. Soc. of Am. Bull.,* 110 (8), 947-971.

Ben-Zion, Y., Z. Peng, D. Okaya, L. Seeber, L. G. Armbruster, N. Ozer, A. J. Michael, S. Baris, and M. Aktar (2003). A shallow fault zone structure illuminated by trapped waves in the Karadere-Duzce branch of the North Anatolian fault, western Turkey, *Geophys. J. Int.,* 152, 699-717, doi:10.1046/j.1365-246X.2003.01870.x.

Brune, J. N., D. von Seggern, and A. Anooshehpoor (2003), Distribution of precarious rocks at the Nevada Test site: Comparison with ground motion predictions from nuclear test, *J. Geophys. Res.*, 108 (B6), 2306, doi:10.1029/2002JB002000.

Cochran, E. S., Y.-G. Li, P. M. Shearer, S. Barbot, Y. Fialko, and J. E. Vidale (2009), Seismic and geodetic evidence for extensive, long-lived fault damage zones, *Geology*, 37, 315-318, doi:10.1130/G25306A.

Day, S. M., L. A. Dalguer, N. Lapusta, and Y. Liu (2005), Comparison of finite difference and boundary integral solutions to three-dimensional spontaneous rupture, *J. Geophys. Res.*, 110, B12307, doi:10.1029/2005JB003813.

Duan, B., and D. D. Oglesby (2006). Heterogeneous fault stresses from previous earthquakes and the effect on dynamics of parallel strike-slip faults, *J. Geophys. Res.*, 111, B05309, doi:10.1029/2005JB004138.

Duan, B., and D. D. Oglesby (2007). Nonuniform prestress from prior earthquakes and the effect on dynamics of branched fault systems, *J. Geophys. Res.*, 112, B05308, doi:10.1029/2006JB004443.

Duan, B., and S. M. Day (2008). Inelastic strain distribution and seismic radiation from rutpure of a fault kink, *J. Geophys. Res.*, 113, B12311, doi:10.1029/2008JB005847.

Duan, B. (2008a). Effects of low-velocity fault zones on dynamic ruptures with nonelastic off-fault response, *Geophys. Res. Lett.*, 35, L04307, doi:10.1029/2008GL033171.

Duan, B. (2008b). Asymmetric off-fault damage generated by bilateral ruptures along a bimaterial interface, *Geophys. Res. Lett.*, 35, L04307, doi:10.1029/2008GL033171.

Hanks, T.C., N.A. Abrahamson, M. Board, D.M. Boore, J.N. Brune, and C.A. Cornell (2006). Report of the workshop on extreme ground motions at Yucca Mountain, August 23-24, 2004, USGS Open-File Report 2006-1277.

Harris, R. A., and S. M. Day (1993). Dynamics of fault interaction: Parallel strike-slip faults, *J. Geophys. Res.*, 98, 4461-4472

Harris, R. A., and S. M. Day (1997). Effects of a low-velocity zone on a dynamic rupture, *Bull. Seismol. Soc. Am.*, 87, 1267-1280.

Harris, R. A., M. Barall, R. Archuleta, et al. (2009). The SCEC/USGS dynamic earthquake rupture code verification exercise, *Seism. Res. Lett.*, 80, 119-126, doi:10.1785/gssrl.80.1.119.

Li, Y. G., K. Aki, D. Adams, A. Hasemi, and W. H. K. Lee (1994), Seismic guided waves trapped in the fault zone of the Landers, California, earthquake of 1992, *J. Geophys. Res.*, 99, 11,705-11,722.

Li, Y. G., J. E. Vidale, S. M. Day, and D. Oglesby (2002), Study of the M7.1 Hector Mine, California, earthquake fault plan by fault-zone trapped waves, *Bull. Seism. Soc. Am.*, 92, 1318-1332.

Ma, S. (2009). Distinct asymmetry in rupture-induced inelastic strain across dipping faults: An off-fault yielding model, *Geophys. Res. Lett.*, 36, L20317, doi:10.1029/2009GL040666.

Oglesby, D. D., D. S. Dreger, R. A. Harris, N. Ratchkovski, and R. Hansen (2004), Inverse kinematic and forward dynamic models of the 2002 Denali Fault earthquake, Alasa, Bull. Seismol. Soc. Am., 94, S214-S233.

Potter, C. J., W. C. Day, D. S. Sweetkind, and R. P. Dickerson (2004). Structure geology of the proposed site area for a high-level radioactive waste repository, Yucca Mountain, Nevada, *Bull. Geol. Soc. Am.* **116**, 858-879.

Ramelli, A. R., J. A. Oswald, G. Vadurro, C. M. Menges, and J. B. Paces (2004), Quaternary faulting on the Solitario Canyon fault, in *Quaternary Paleoseismology and Stratigraphy of the Yucca Mountain Area, Nevada*, W. R. Keefer, J. W. Whitney and E. M. Taylor (Editors), *U.S. Geol. Surv. Profess. Pap.* 1689, 89-110.

Rice, J. R., and M. P. Cleary (1976). Some basic stress diffusion solutions for fluid-saturated elastic porous media with compressible constituents, *Rev. Geophys.*, 14, 227-241.

Somerville, P. G., N. F. Smith, R. W. Graves, N. A. Abrahamson (1997), Modification of empirical strong ground motion attenuation relations to include the amplitude and duration effects of rupture directivity, *Seismol. Res. Lett.*, 68, 199-222.

Stepp, J.C., I. Wong, J.Whitney, R. Quittmeyer, N. Abrahamson, G. Toro, R. Youngs, K. Coppersmith, J. Savy, T. Sullivan and Yucca Mountain PSHA project members (2001). Probabilistic seismic hazard analyses for ground motions and fault displacements at Yucca Mountain, *Earthquake Spectra* **17**, 113-151.

Stock, J. M., J. H. Healy, S. H. Hickman, and M. D. Zoback (1985), Hydraulic fracturing stress measurements at Yucca Mountain, Nevada, and relationship to the regional stress field, *J. Geophys. Res.*, 90, 8691-8706.

Templeton, E.L., H.S. Bhat, R. Dmowska, and J.R. Rice (2010). Dynamic rupture through a branched fault configuration at Yucca Mountain and resulting ground motions, *Bull. Seism. Soc. Am.*, in press.

Department of Geology & Geophysics
Texas A&M University
College Station, Texas 77843
(B.D.)

Department of Geological Sciences
San Diego State University,
San Diego, California 92182
(S.M.D.)

Table 1. Fault models in this study

MODEL	DESCRIPTION
PLWOFZ	Planar fault, without fault zone
PLWFZ	Planar fault, with a 100-m-wide low-velocity fault zone
KNWOFZ	Kink fault with a change in dip at -1 km depth, without fault zone
KN2WOFZ	Kink fault with two changes in dip at -1 km and -6 km depths, without fault zone
KNWFZ	Kin fault with a change in dip at -1 km depth and the fault zone

Table 2. Layer Properties in the Model of PLWFZ*

Unit	ρ (kg/m^3)	*Vp* (m/s)	*Vs* (m/s)	ν	$tan\varphi$	*C* (MPa)
Topopah, unsaturated, wall rock	2250	3610	2210	0.2	1.0	10
Topopah, unsaturated, fault zone	2250	2888	1768	0.2	0.8	1
Topopah, saturated, wall rock	2400	4135	2210	0.3	1.0	10
Topopah, saturated, fault zone	2400	3308	1768	0.3	0.8	1
Calico, unsaturated, wall rock	1700	2961	1900	0.15	0.75	1
Calico, unsaturated, fault zone	1700	2369	1520	0.15	0.75	1
Calico, saturated, wall rock	1900	3555	1900	0.3	0.75	1
Calico, saturate, fault zone	1900	2844	1520	0.3	0.75	1
Prow Pass, unsaturated, wall rock	2000	3511	2150	0.2	0.85	5
Prow Pass, unsaturated, fault zone	2000	2809	1720	0.2	0.75	1
Prow Pass, saturated, wall rock	2150	4022	2150	0.3	0.85	5
Prow Pass, saturated, fault zone	2150	3218	1720	0.3	0.75	1
Paleozoic dolomite, wall rock	2700	5712	3298	0.25	1.0	100
Paleozoic dolomite, fault zone	2700	4570	2638	0.25	0.8	10
Deeper crust, wall rock	2700	6200	3580	0.25	1.0	100
Deeper crust, fault zone	2700	4960	2864	0.25	0.8	10

*Property values for the layers outside of the fault zone are adopted from Andrews et al. (2007). For the low-velocity fault zone, we keep the density and Poisson's ratio the same in each unit, but seismic velocities *Vp* and *Vs* are reduced by 20% and internal friction and cohesion may also decrease.

Figure Captions

Figure 1. Color orthophoto map of the Yucca Mountain area with surface fault traces. Numbers show locations of observed maximum-surface-slip values of 1.3 m on the Solitario Canyon fault, 0.4 m on the Fatigue Wash fault, and 1.0 m on the Windy Wash fault. The surface traces of these three faults merge toward the south and they are likely one fault at depth. (From Andrews et al., 2007, Figure 7).

Figure 2. A seismic profile with interpretation. The dip of the Solitario Canyon fault becomes shallower below about 1 km from the ground surface. (From Brocher et al., 1998, Figure 13).

Figure 3. Different fault models in this study to examine effects of fault geometry and fault zone structure of the Solitario Canyon fault (black line) on ground motion at the repository site (plus sign). (a) PLWOFZ and (b) PLWFZ are planar fault models, while (c) KNWOFZ and (d) KNWFZ are kinked fault models with a change in dip from 60° to 50° at depth of 1 km. Fault zone is absent in (a) and (c), while a 100-m wide fault zone bisected by the fault is present in (b) and (d). In the fault zone, seismic wave velocities (both P and S) of rock are reduced 20% relative to those of corresponding wall rock of the same geologic unit.

Figure 4. Closer view of the geologic structure in the model of PLWFZ (Figure 3b). A 100-m wide low-velocity fault zone with a reduction in seismic velocities of 20% relative to wall rock is present in this model.

Figure 5. Stresses (left panel) and final slip (right panel) on the modeled Solitario Canyon fault with a possible maximum slip of about 15 m at the surface. Initial frictional strength is a product

of the static frictional coefficient (0.7) and normal stress. Results from calculations with off-fault elastic response (E/ Elastic) and off-fault elastoplastic response (P/Plastic) are compared.

Figure 6. Time histories of ground velocity at the site with and without plastic yielding for the maximum possible surface slip of ~ 15 m from this study (left panels) and from Andrews et al (2007) (right panels). Both waveforms and peaks are very close to each other between the two studies.

Figure 7. Stresses (left) and final slip (right) on the Solitario Canyon fault in a set of simulations with surface slip of ~ 5 m. Initial strength is different for sub-Rayleigh (R) and supershear (S) ruptures, while initial shear stress is the same. Large peak or trough in final shear stress in the cases of elastoplastic (P) off-fault response is caused by plastic yielding, which is absent in the cases of elastic (E) off-fault response.

Figure 8. Time histories of ground velocity at the site from (a) this study and (b) Andrews et al. (2007). Left and right panels are results from sub-Rayleigh and supershear ruptures, respectively. Light and heavy curves are for elastic and elastoplastic calculations, respectively. Results from the two studies are comparable. See text for details.

Figure 9. Plastic strain distributions in three rupture scenarios with off-fault elastoplastic response. The plus sign denotes the repository site. Plastic yielding only occurs at shallow depth, which results in reduced fault slip near the free surface shown in Figures 5 and 7.

Figure 10. Comparison of time histories (a) and (b) of ground velocity at the site with two different element sizes and the distribution of plastic strain (c) with the coarse element size of 25 m in the case of 5-m-slip, sub-Rayleigh rupture with off-fault elastoplastic response.

Figure 11. Effects of time-dependent pore fluid pressure (dynamic p) on ground motion at the site in the 15-m-slip case (left panels) and the case of 5-m-slip, sub-Rayleigh rupture (right panels), with off-fault elastoplastic response. Compared with ground motion with a constant pressure (static p), effects of time-dependent pore pressure are minor.

Figure 12. Plastic strain distribution with time-dependent pore pressure (dynamic p) in the 15-m-slip (a) and 5-m-slip, sub-Rayleigh rupture (c) cases, and comparison of final slip on the SCF in calculations with constant pore pressure (static p) and time-dependent pore pressure for the 15-m-slip (b) and 5-m-slip, sub-Rayleigh rupture (d) cases. In both elastic and elastoplastic calculations, time-dependent pore pressure results in larger slip at shallow depth. Time-dependent pore pressure results in more yielding on the footwall of the SCF in the 15-m-slip case, compared with that with constant pore pressure (Figure 9a).

Figure 13. Stresses (left panel) and final slip (right panel) on the modeled Solitario Canyon fault with a deeper seismogenic depth. The seismogenic depth is defined as the maximum depth of shear stress drop and it is -13.5 km (15.6 km down-dip distance) in these models, while it is -12 km (13.9 km down-dip distance) in the previous 15-m-slip models. The deeper seismogenic depth results in larger fault slip.

Figure 14. Effects of the seismogenic depth on ground velocity at the site in the 15-m-slip case. A deeper seismogenic depth does not affect earlier peaks in ground velocity but increase later

peaks. Ground velocities for the "shallow" seismogenic depth are those from the 15-m-slip case in Section 5.1 with time-dependent pore pressure. See text for details of the "deep" seismogenic depth case.

Figure 15. Effects of shallower dips of the SCF at depth on ground velocity at the site in the 15-m-slip case. The effect is profound when off-fault response is elastic. See text for details about the models.

Figure 16. Effects of shallower dips of the SCF at depth on ground velocity at the site in the 5-m-slip case. See text for details.

Figure 17. Plastic strain distribution from the model KNWOFZ in the cases of (a) 5-m-slip and (b) 15-m-slip, and (c) final fault slip from PLWOFZ, KNWOFZ and KN2WOFZ with elastic off-fault response in the 5-m-slipcase. Given the same depth profile of initial stress distribution, shallower dips of the SCF at depth result in longer ruptured fault lengths and thus larger fault slips. Shallower dips also result in more extensive plastic yielding.

Figure 18. Sensitivity of ground velocity at the site to cohesion of shallow geologic units in the 15-m-slip case from two models PLWOFZ and KNWOFZ. C represent calculations with cohesion values in Table 2, while DC represent calculations with doubled cohesion values in shallow units. See text for details.

Figure 19. Plastic strain distribution in the model KNWOFZ with doubled cohesion values in shallow units (left panels) and sensitivity of ground velocity at the site to the cohesion variation

in the 5-m-slip case from the model KNWOFZ (right panels). See the caption of Figure 18 for explanations of the legend for ground motions.

Figure 20. Effects of a hypothetical 100-m wide low-velocity fault zone of the SCF on ground motion at the repository site in the 15-m-slip scenarios.

Figure 21. Effects of a hypothetical 100-m wide low-velocity fault zone of the SCF on ground motion at the repository site in the 5-m-slip scenarios.

Figure 22. A summary plot of peak ground velocity, shown as a function of surface fault slip, from our simulations (color symbols) and Andrews et al. (2007) (black symbols). C and DC represent calculations with cohesion values in Table 2 and with doubled cohesion values for shallow units (see text for details), respectively. The degree of shading in color symbols correlates with cohesion values in calculations: Dark shading for C (reference cohesion), light shading for DC (doubled cohesion), and open for elastic (very high cohesion). Dashed lines are envelopes of PGV estimates with off-fault yielding.

Figure 23. Spectral acceleration Sa for periods of (a) 0.1 second, (b) 0.3 second, (c) 1.0 second, and (d) 3.0 second, as a function of surface fault slip from our simulations. A critical damping ratio of 0.05 is used. See the caption of Figure 22 for details of symbols.

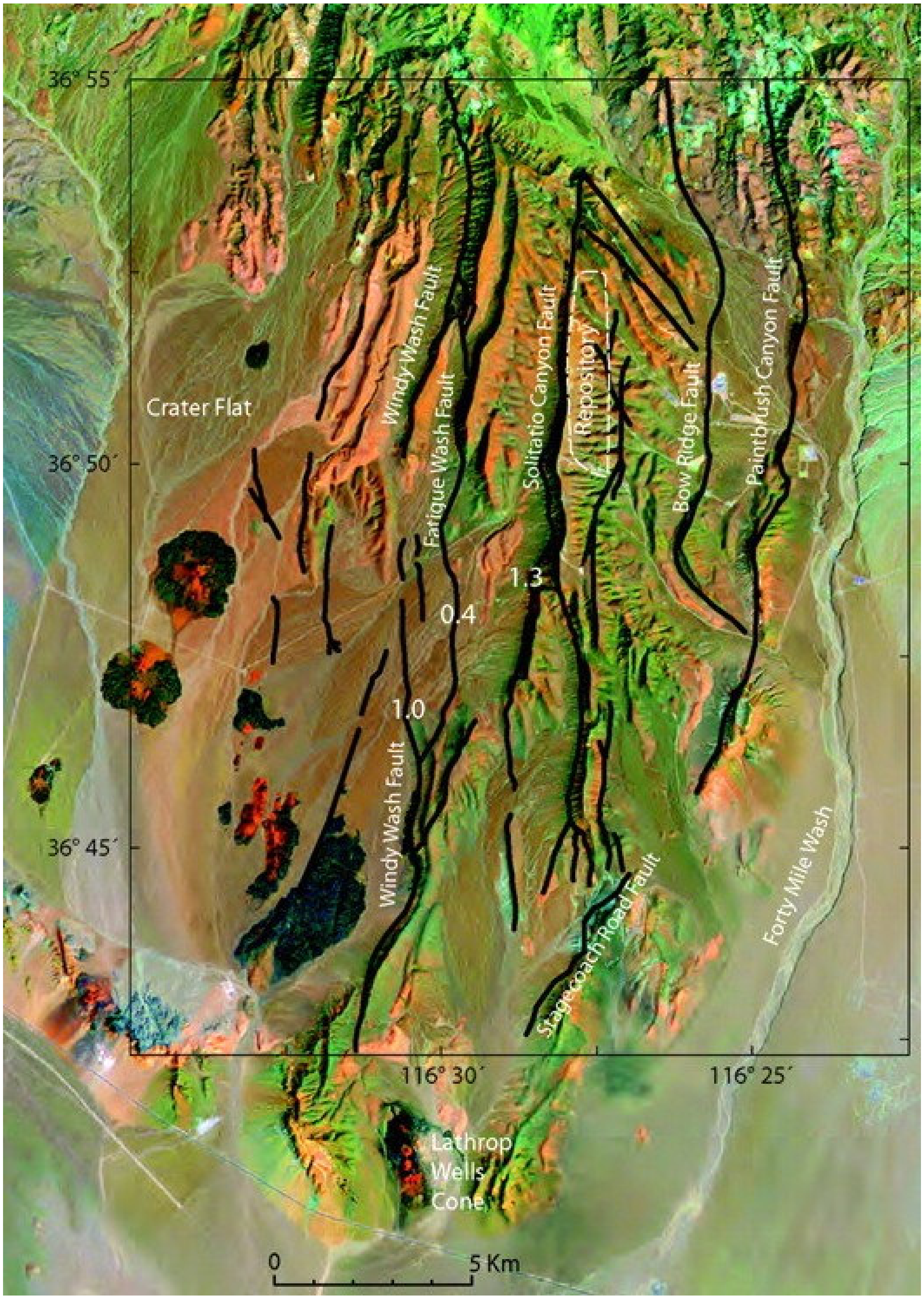
36° 55′
36° 50′
36° 45′
116° 30′
116° 25′
Crater Flat
Windy Wash Fault
Fatigue Wash Fault
Solitratio Canyon Fault
Repository
Bow Ridge Fault
Paintbrush Canyon Fault
1.3
0.4
1.0
Windy Wash Fault
Stagecoach Road Fault
Forty Mile Wash
Lathrop
Wells
Cone
0
5 Km

Figure 1

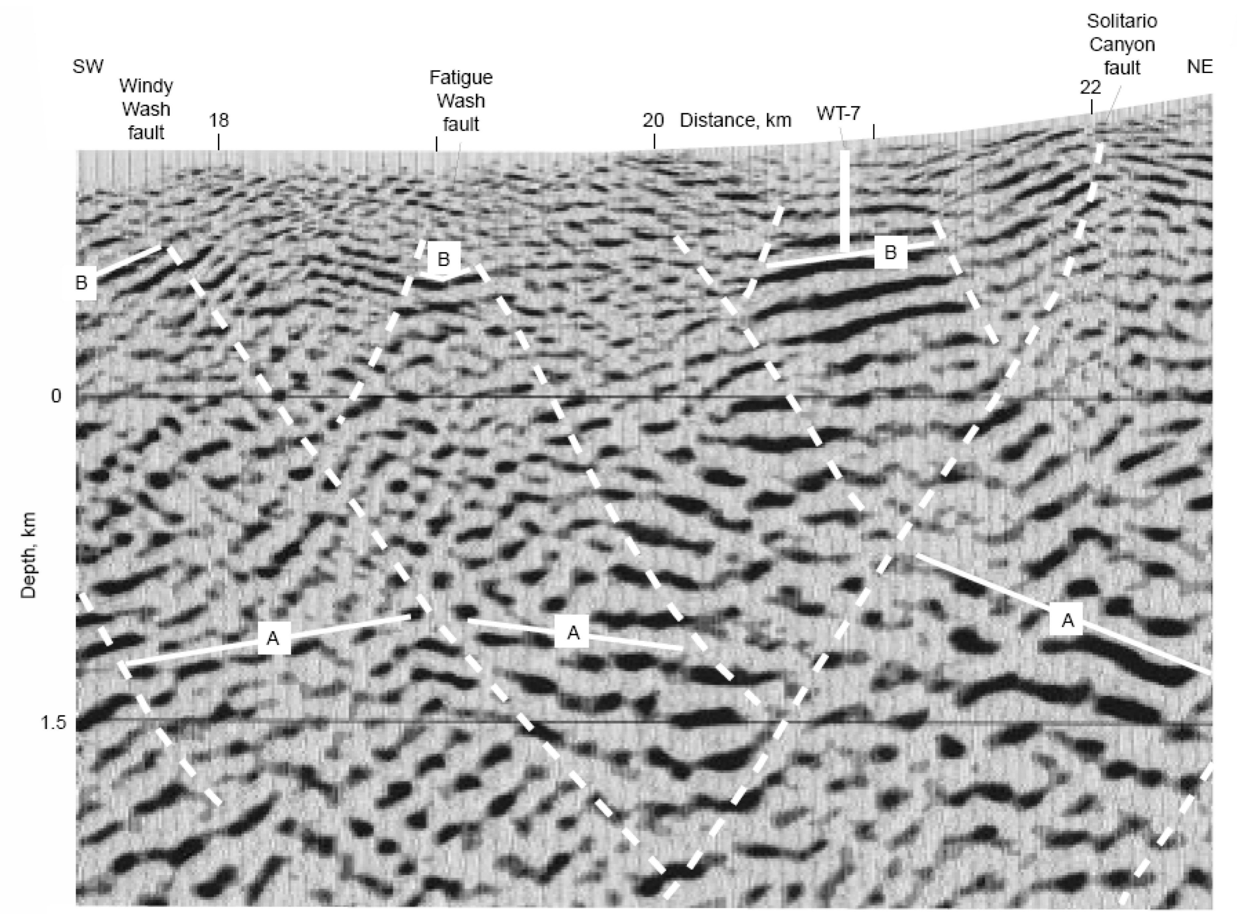
SW
Windy Wash fault
18
Fatigue Wash fault
20
Distance, km
WT-7
Solitario Canyon fault
22
NE
B
B
B
A
A
A
0
1.5
Depth, km

Figure 2

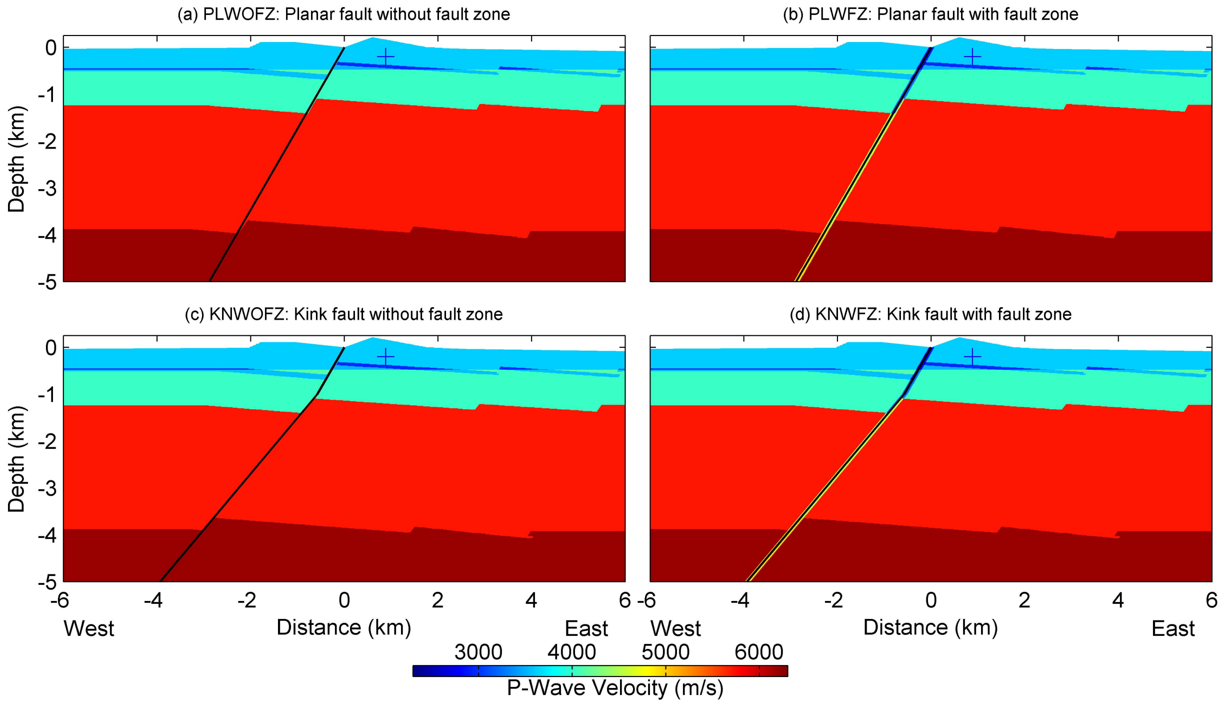

876

877 Figure 3

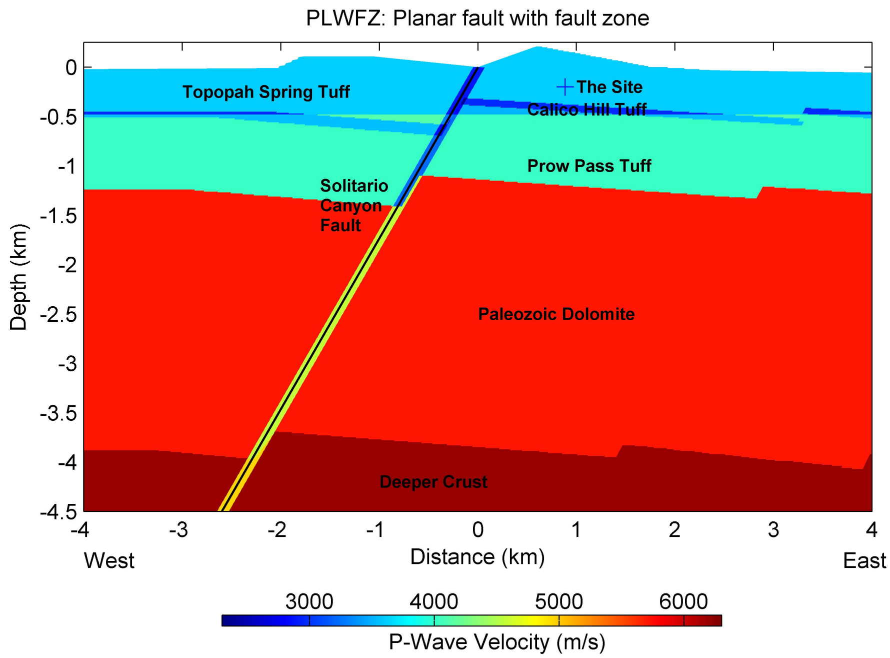
PLWFZ: Planar fault with fault zone
Topopah Spring Tuff
The Site
Calico Hill Tuff
Prow Pass Tuff
Solitario
Canyon
Fault
Paleozoic Dolomite
Deeper Crust
Depth (km)
0
-0.5
-1
-1.5
-2
-2.5
-3
-3.5
-4
-4.5
-4
-3
-2
-1
0
1
2
3
4
West
Distance (km)
East
3000
4000
5000
6000
P-Wave Velocity (m/s)

Figure 4

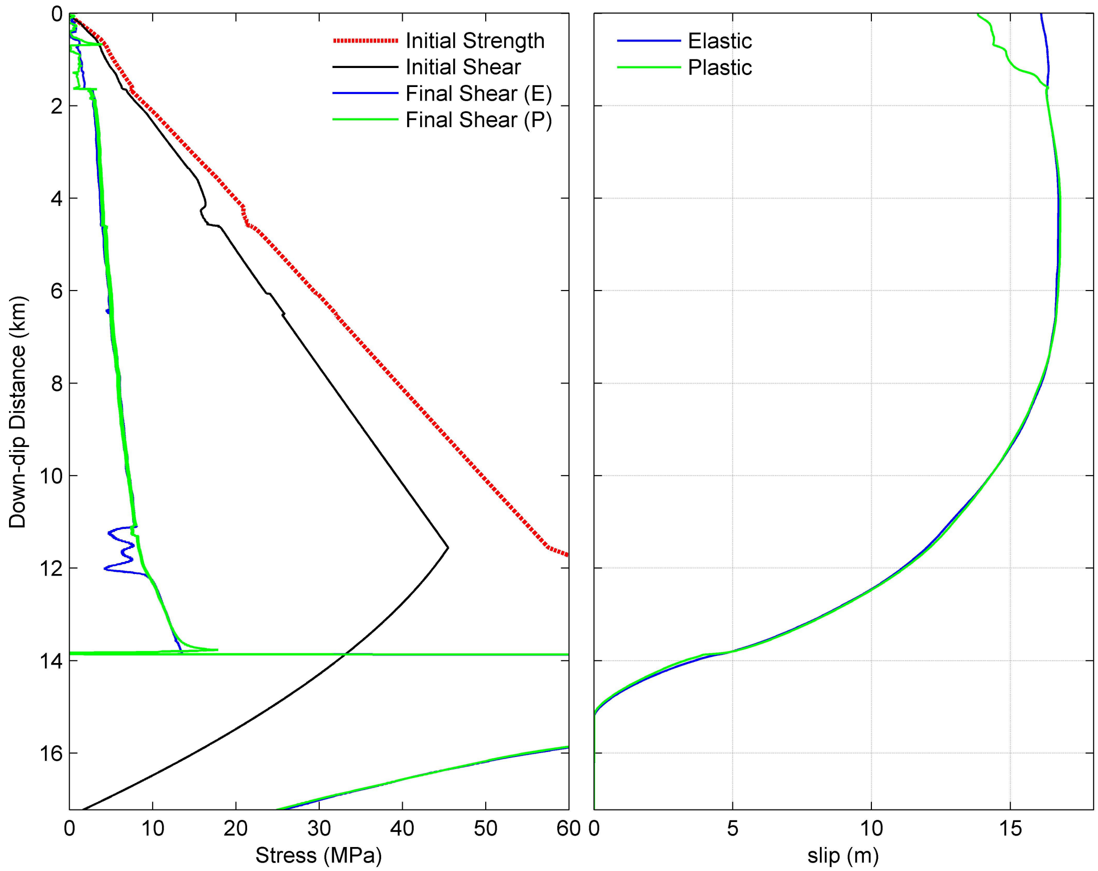
Initial Strength
Initial Shear
Final Shear (E)
Final Shear (P)
Down-dip Distance (km)
Stress (MPa)
Elastic
Plastic
slip (m)
0
2
4
6
8
10
12
14
16
0
10
20
30
40
50
60
0
5
10
15

Figure 5

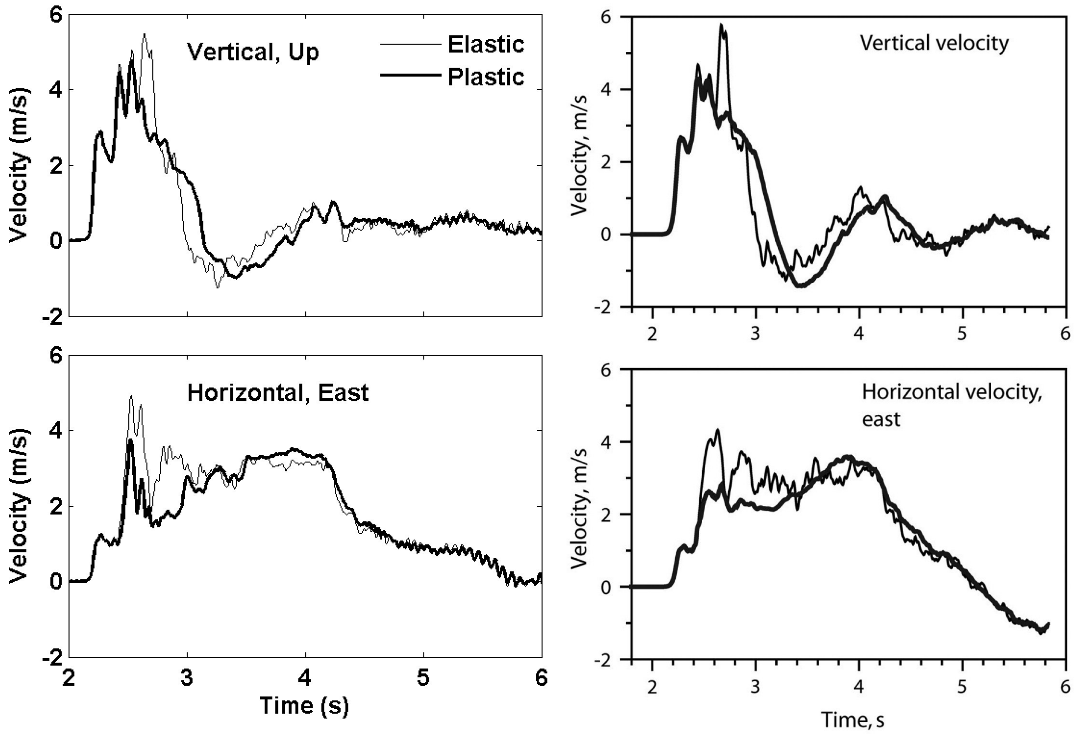
Vertical, Up
Elastic
Plastic
Velocity (m/s)
Horizontal, East
Time (s)
Vertical velocity
Velocity, m/s
Horizontal velocity, east
Time, s

883 Figure 6

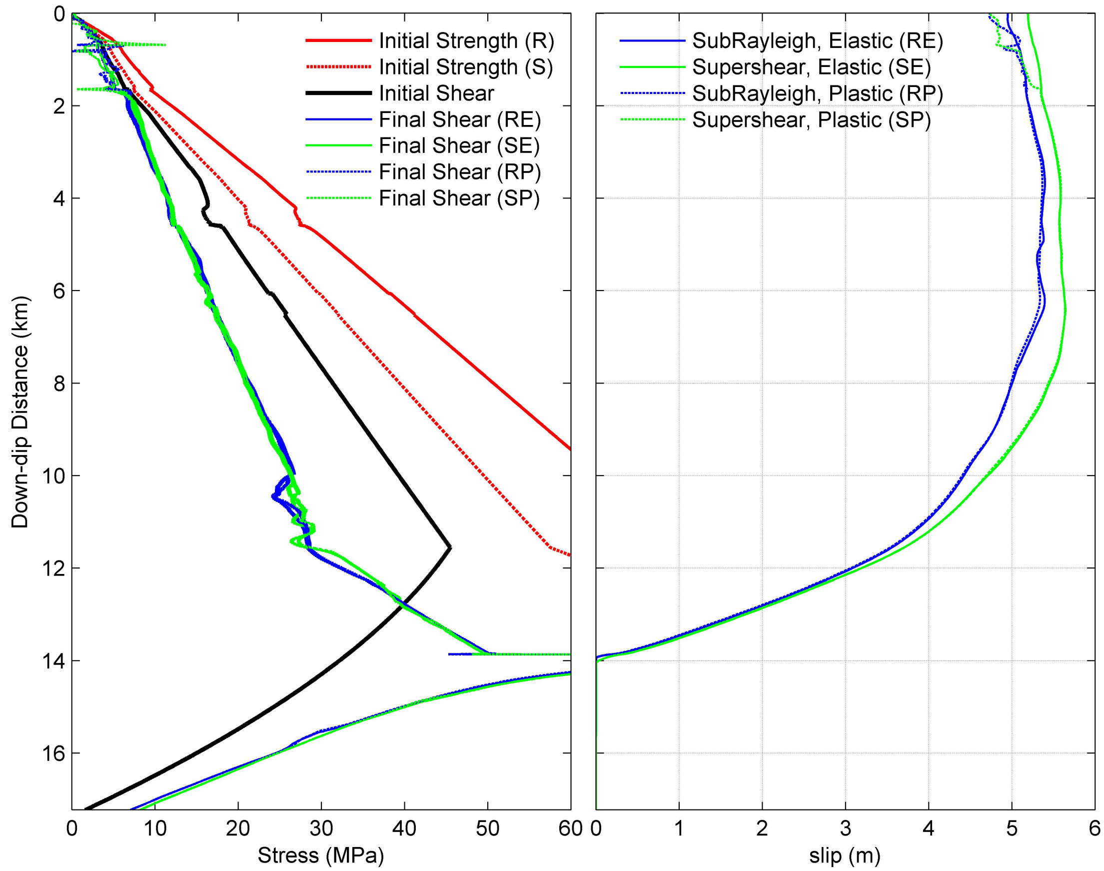

884

885 Figure 7

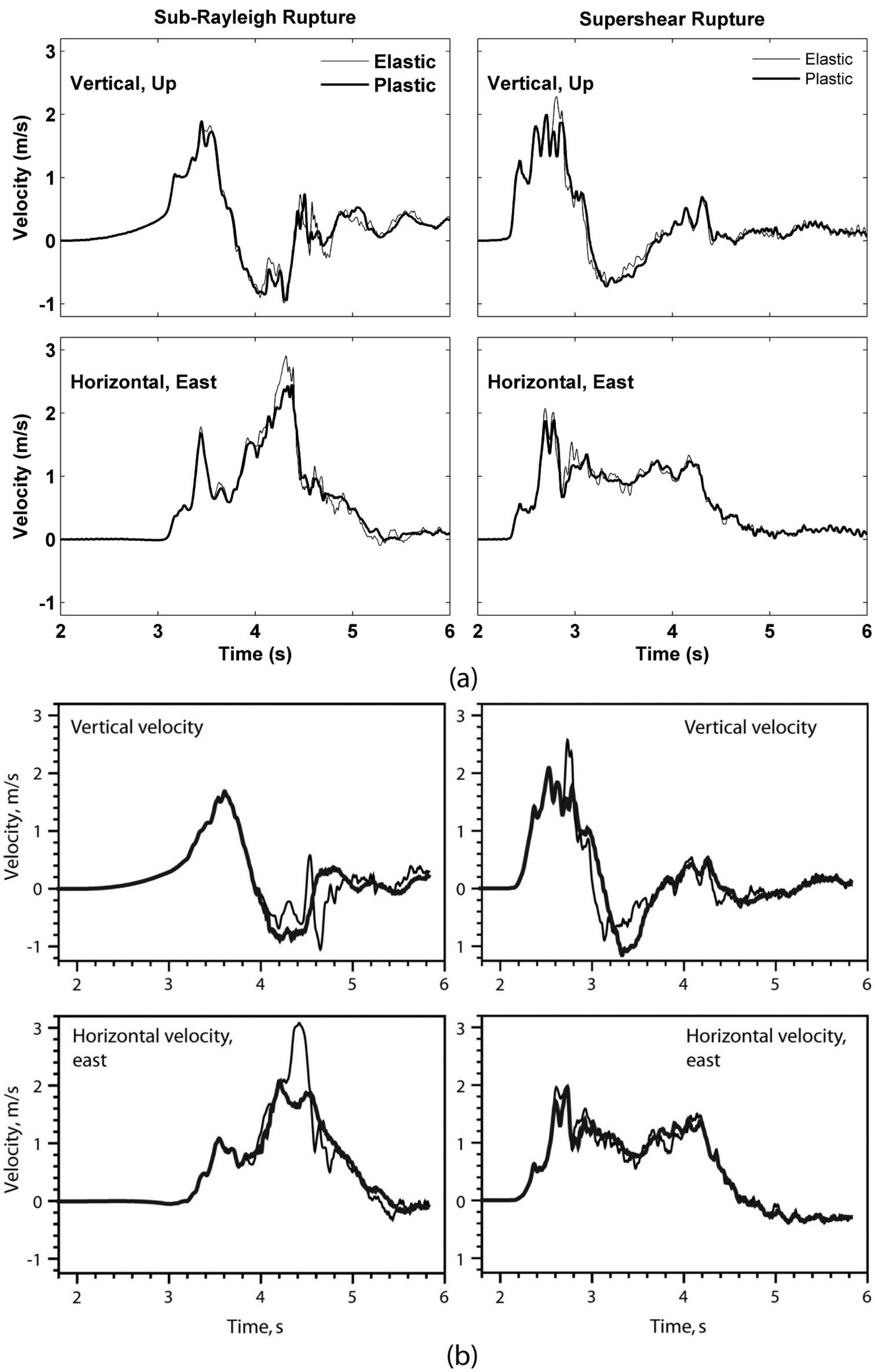
Sub-Rayleigh Rupture
Supershear Rupture
Vertical, Up
Elastic
Plastic
Horizontal, East
Velocity (m/s)
Time (s)
(a)
Vertical velocity
Horizontal velocity, east
Velocity, m/s
Time, s
(b)

Figure 8

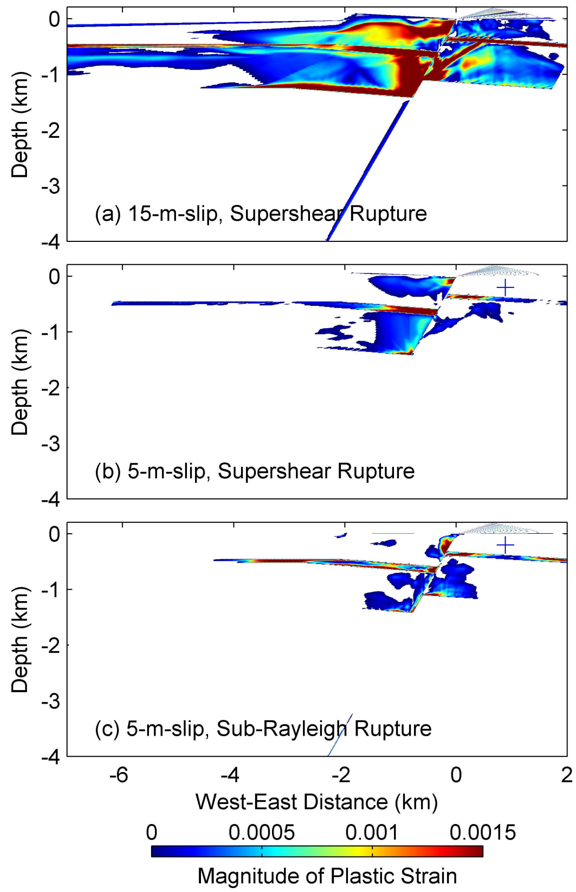
0
-1
-2
-3
-4
Depth (km)
(a) 15-m-slip, Supershear Rupture
(b) 5-m-slip, Supershear Rupture
(c) 5-m-slip, Sub-Rayleigh Rupture
-6
-4
-2
0
2
West-East Distance (km)
0
0.0005
0.001
0.0015
Magnitude of Plastic Strain

Figure 9

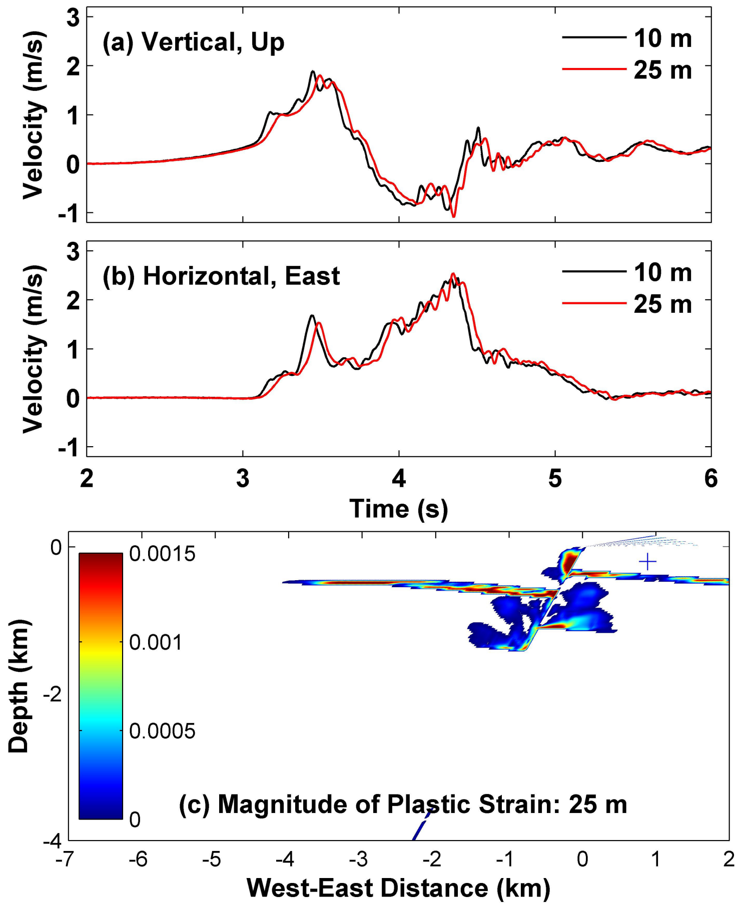

890

891 Figure 10

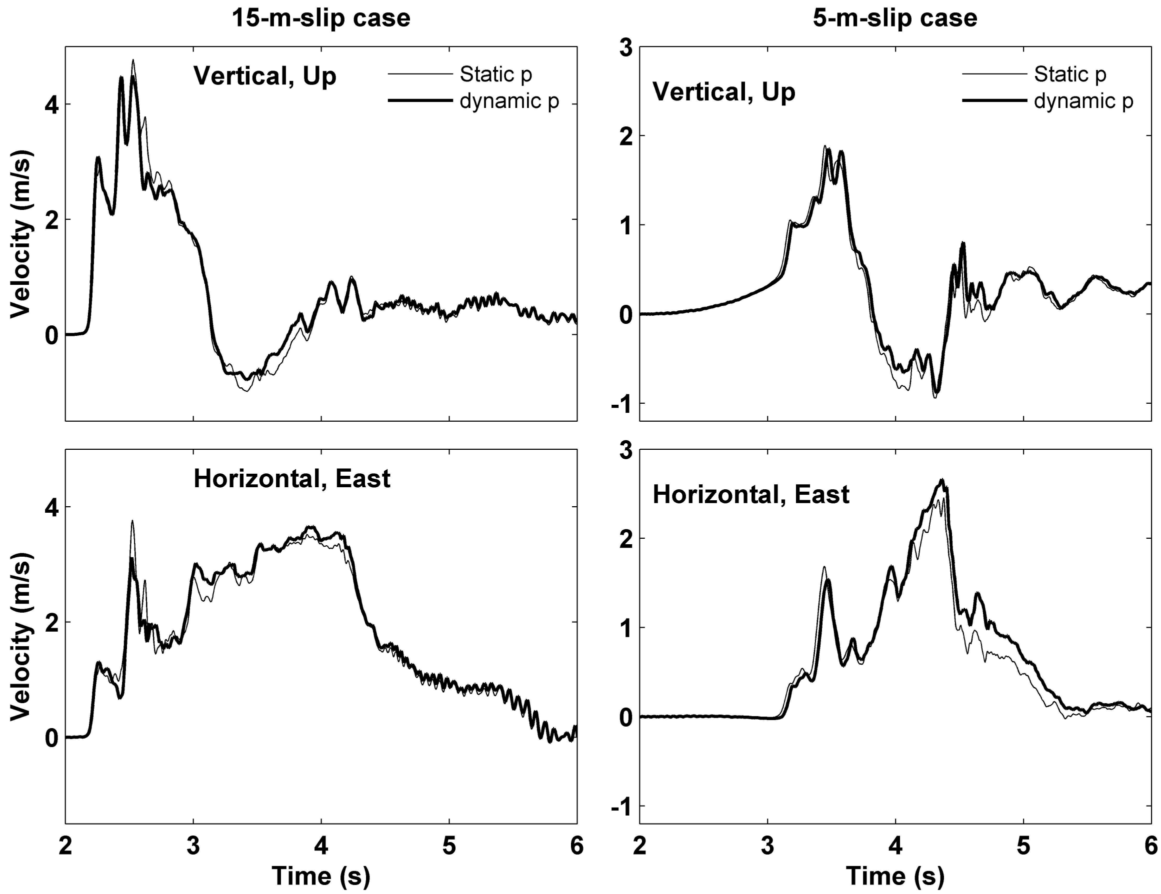

892

893 Figure 11

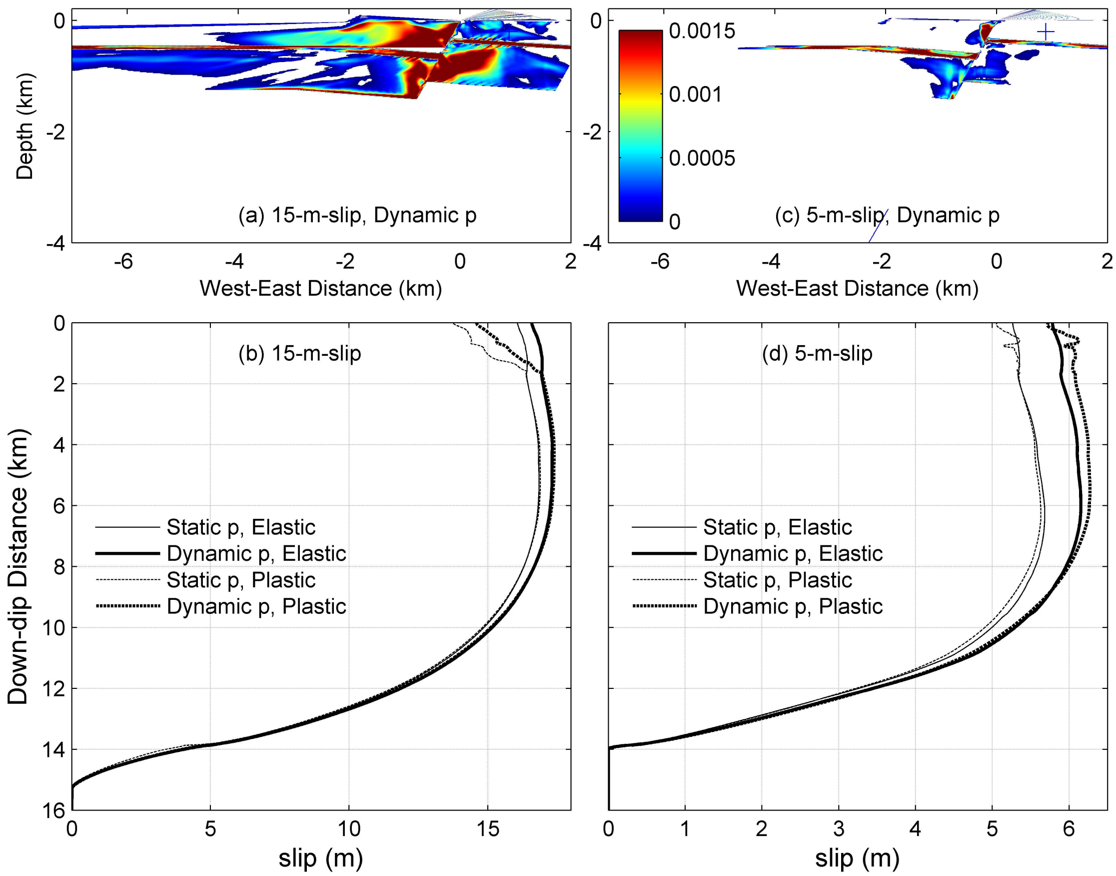
(a) 15-m-slip, Dynamic p
Depth (km)
West-East Distance (km)
(c) 5-m-slip, Dynamic p
0.0015
0.001
0.0005
0
(b) 15-m-slip
(d) 5-m-slip
Down-dip Distance (km)
Static p, Elastic
Dynamic p, Elastic
Static p, Plastic
Dynamic p, Plastic
slip (m)

Figure 12

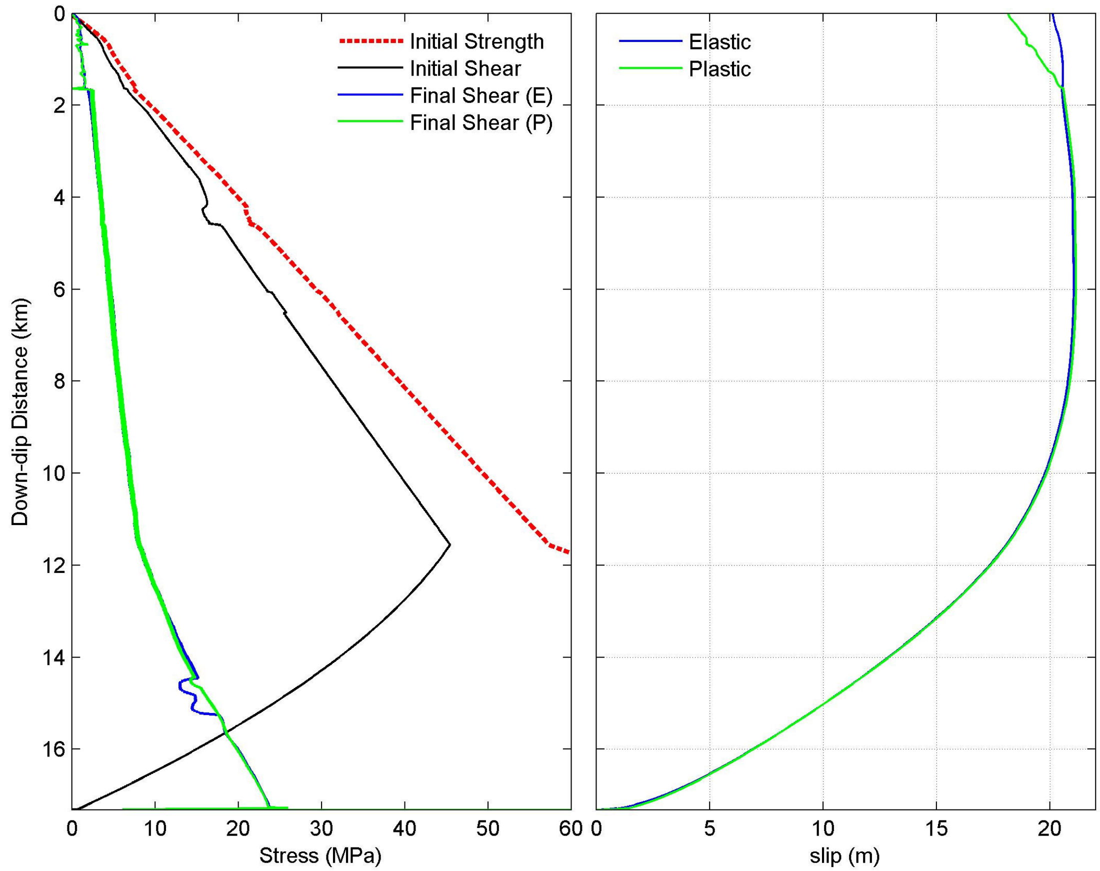

896

897 Figure 13

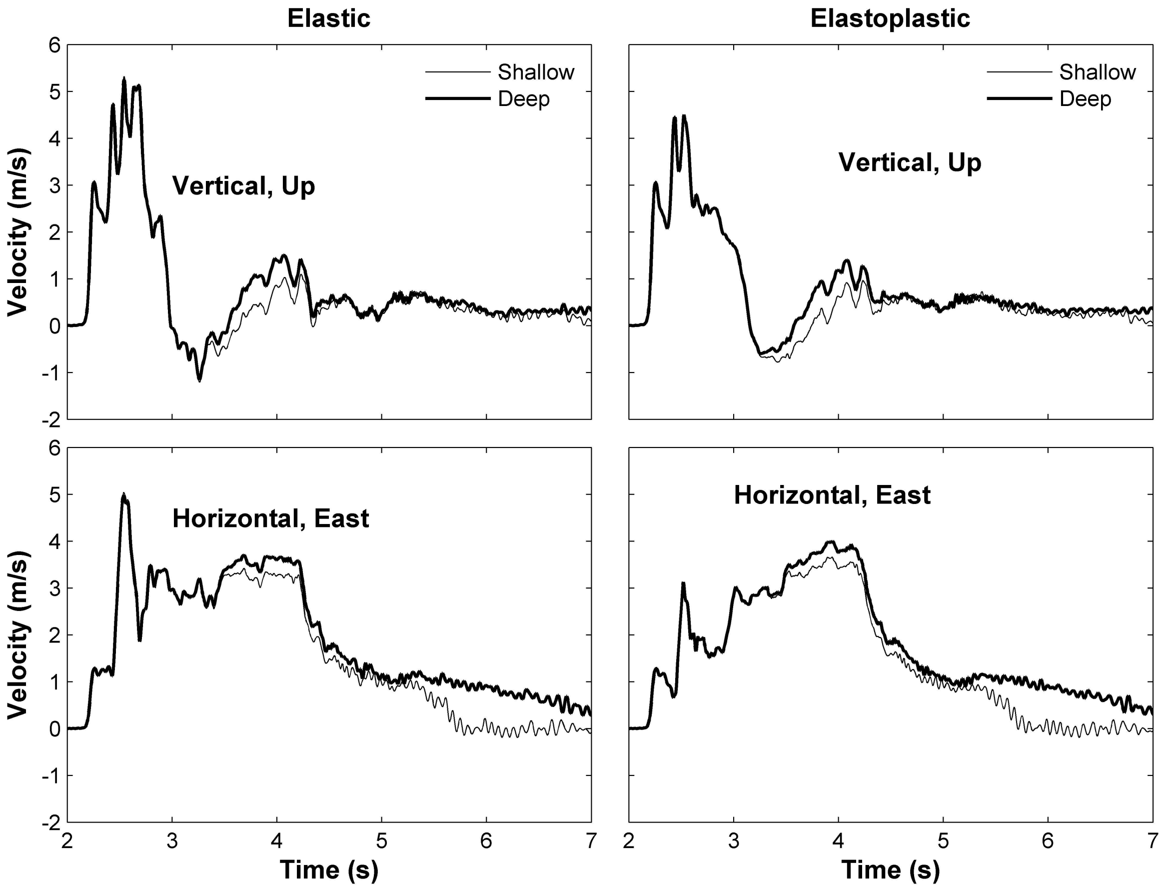
Elastic
Elastoplastic
Shallow
Deep
Vertical, Up
Horizontal, East
Velocity (m/s)
Time (s)

Figure 14

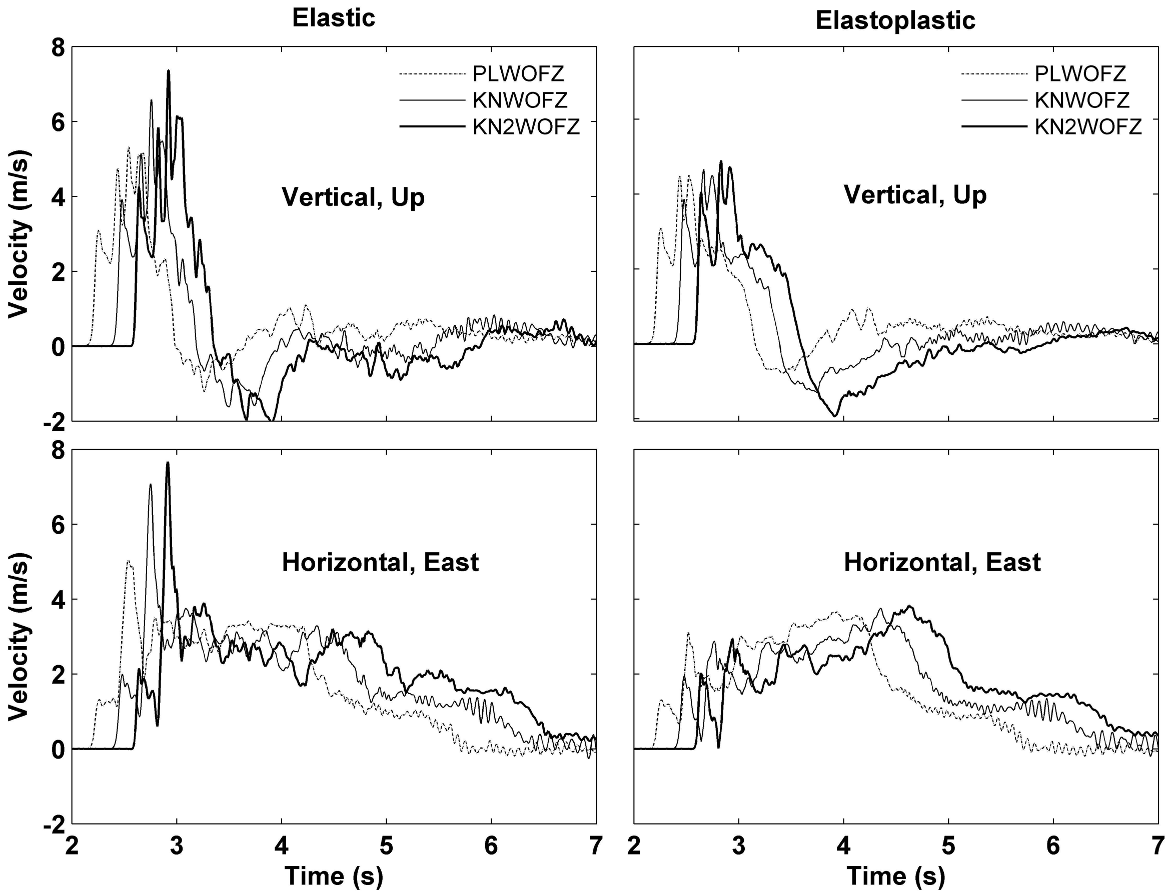

Elastic
Elastoplastic
PLWOFZ
KNWOFZ
KN2WOFZ
Vertical, Up
Horizontal, East
Velocity (m/s)
Time (s)
8
6
4
2
0
-2
2
3
4
5
6
7

Figure 15

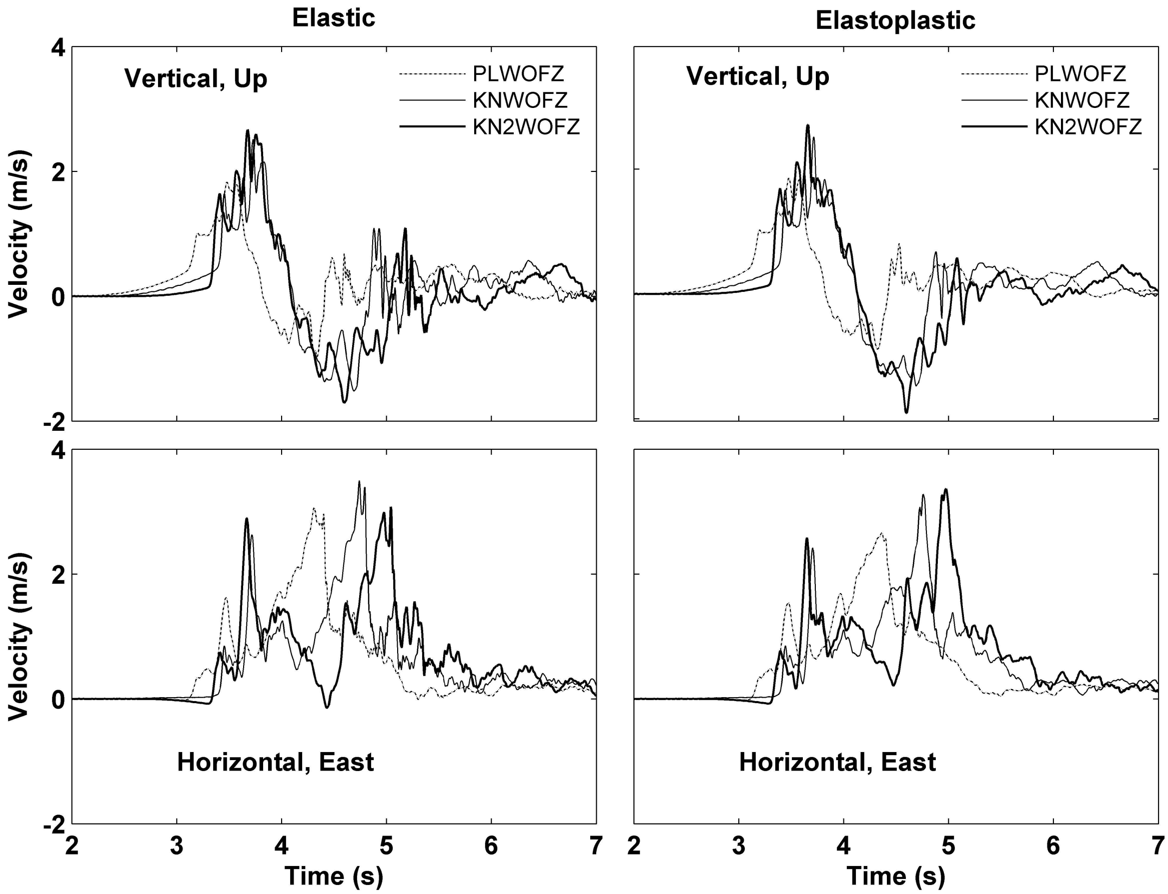
Elastic
Elastoplastic
Vertical, Up
Vertical, Up
PLWOFZ
KNWOFZ
KN2WOFZ
Velocity (m/s)
Horizontal, East
Horizontal, East
Time (s)
Time (s)

Figure 16

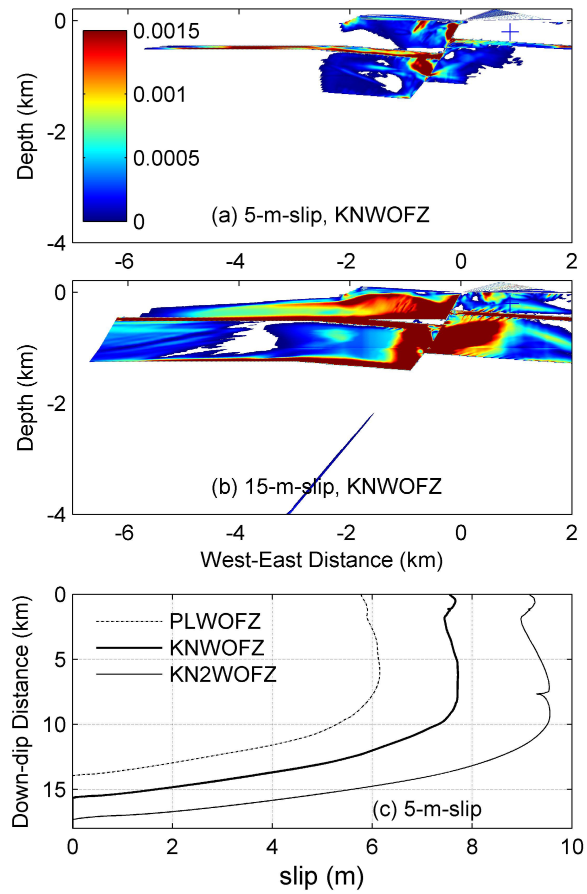

904

905 Figure 17

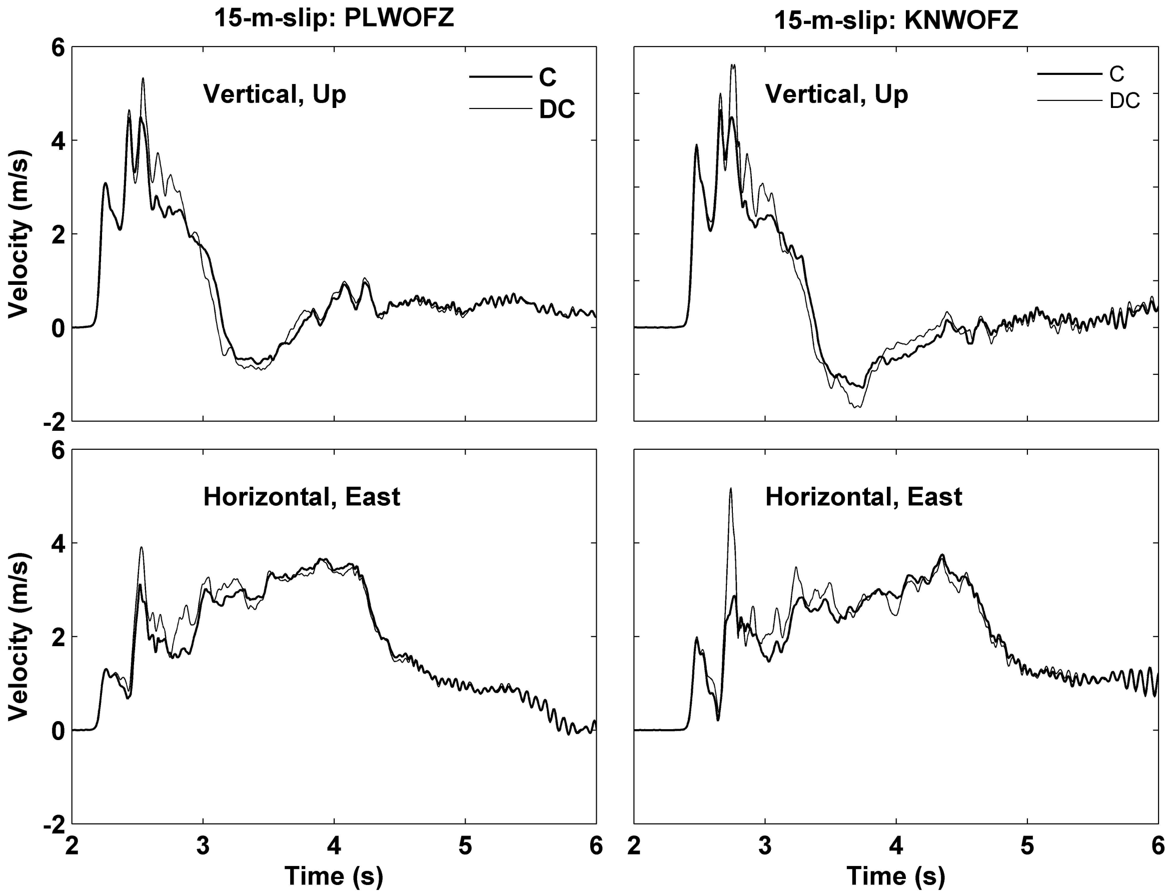
15-m-slip: PLWOFZ
15-m-slip: KNWOFZ
Vertical, Up
Horizontal, East
C
DC
Velocity (m/s)
Time (s)

Figure 18

908

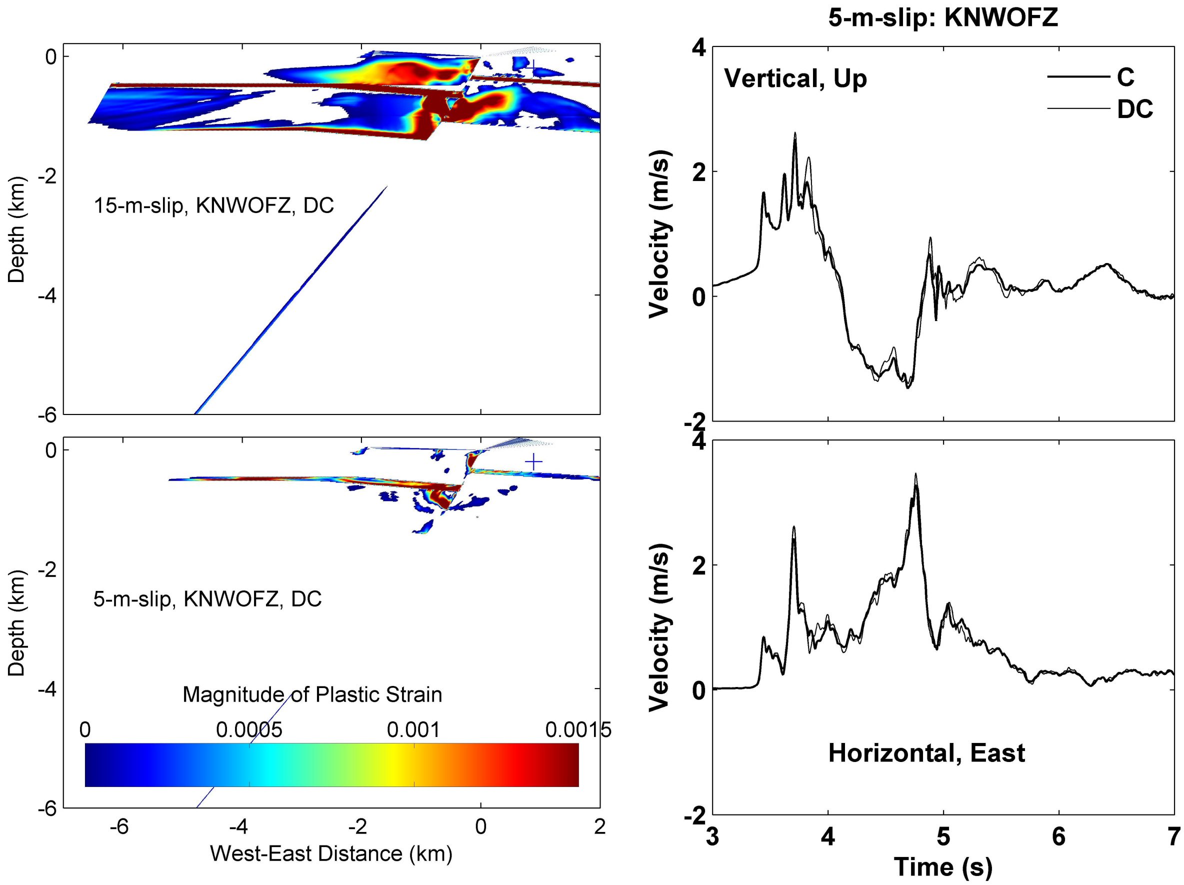

909 Figure 19

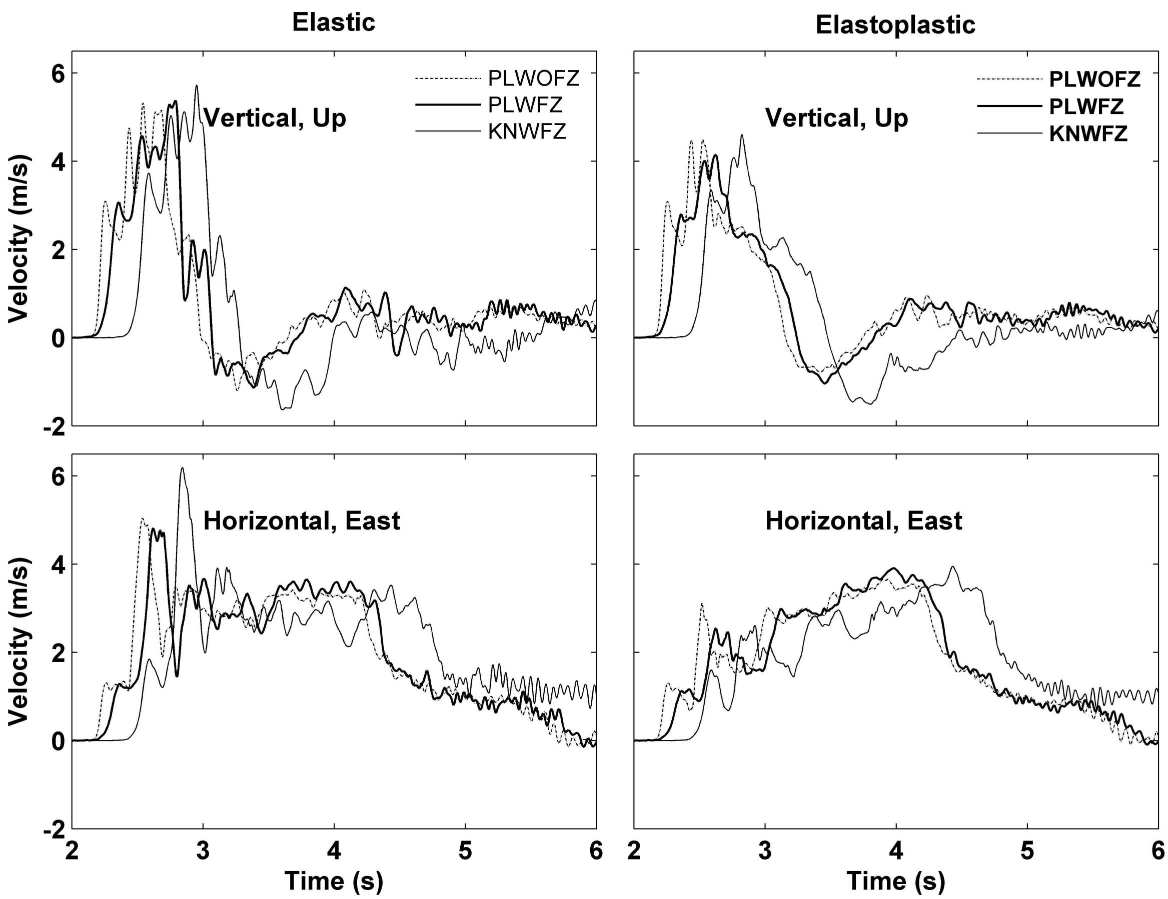
Elastic
Elastoplastic
PLWOFZ
PLWFZ
KNWFZ
Vertical, Up
Horizontal, East
Velocity (m/s)
Time (s)
6
4
2
0
-2
2
3
4
5
6

Figure 20

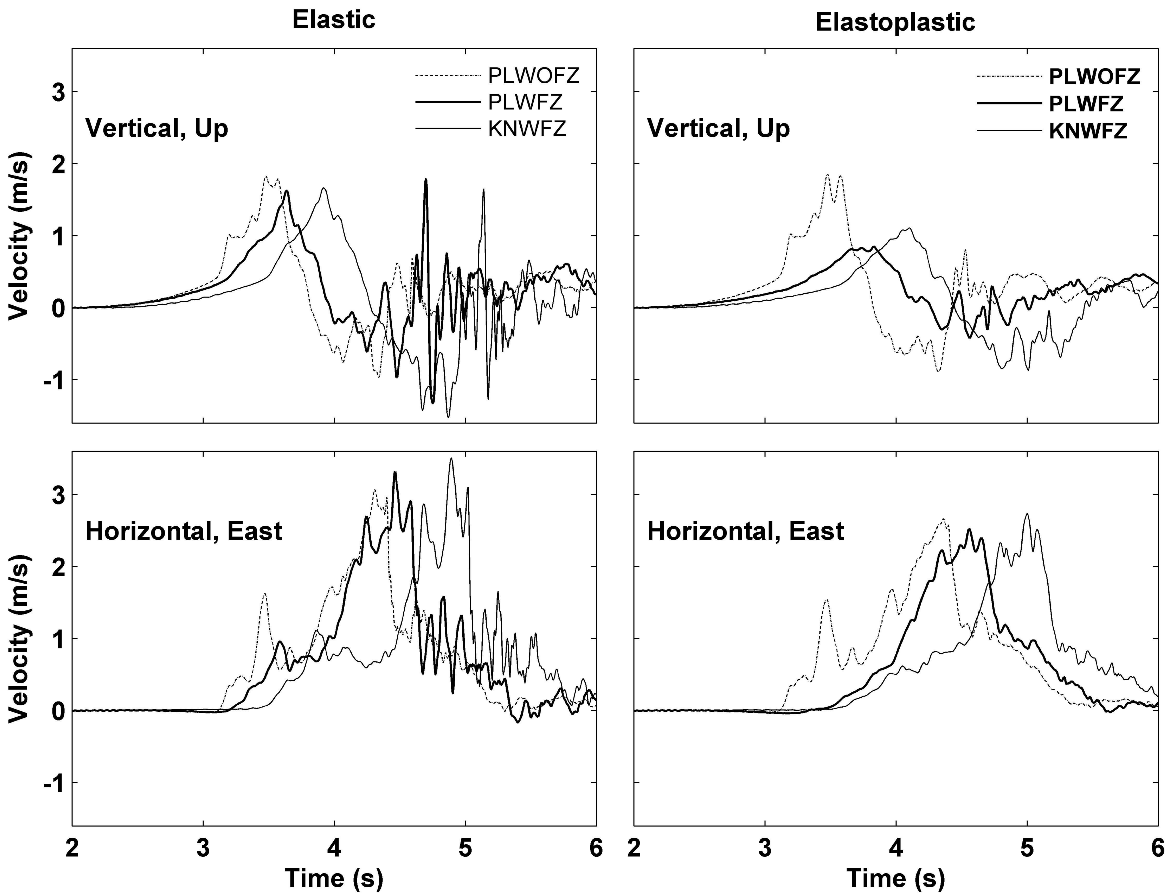
Elastic
Elastoplastic
PLWOFZ
PLWFZ
KNWFZ
Vertical, Up
Horizontal, East
Velocity (m/s)
Time (s)
3
2
1
0
-1
2
3
4
5
6

Figure 21

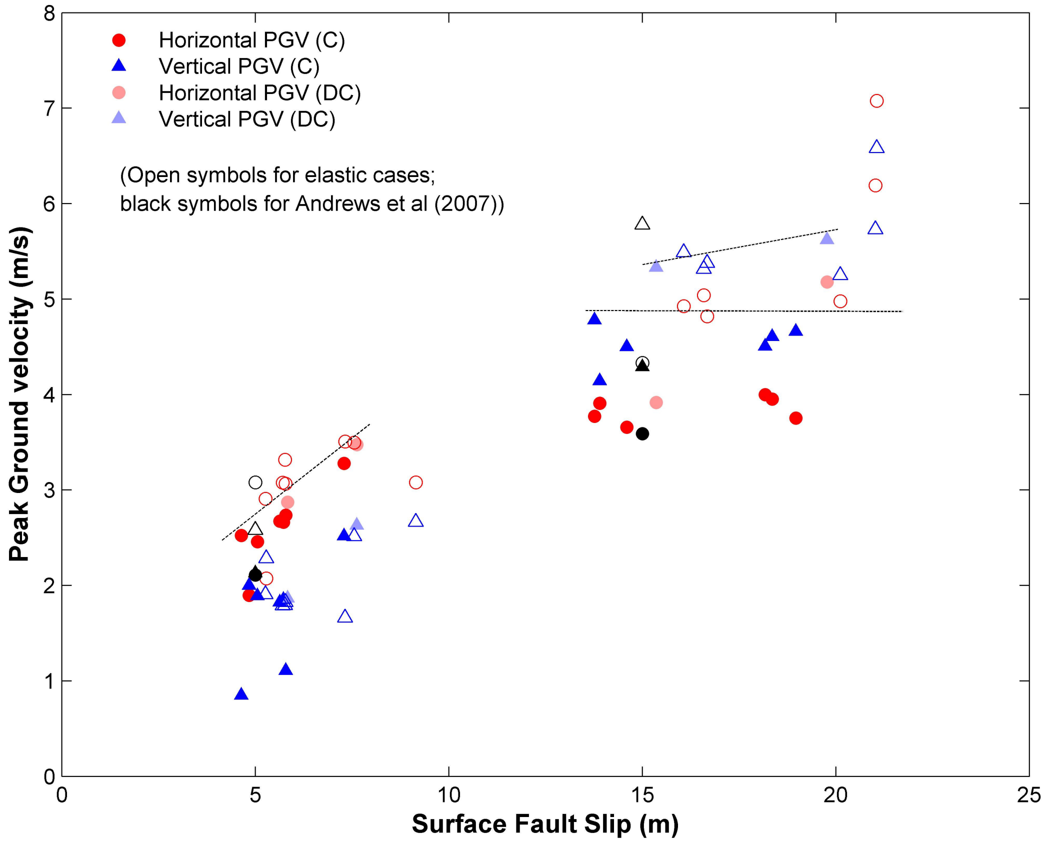

914

915 Figure 22

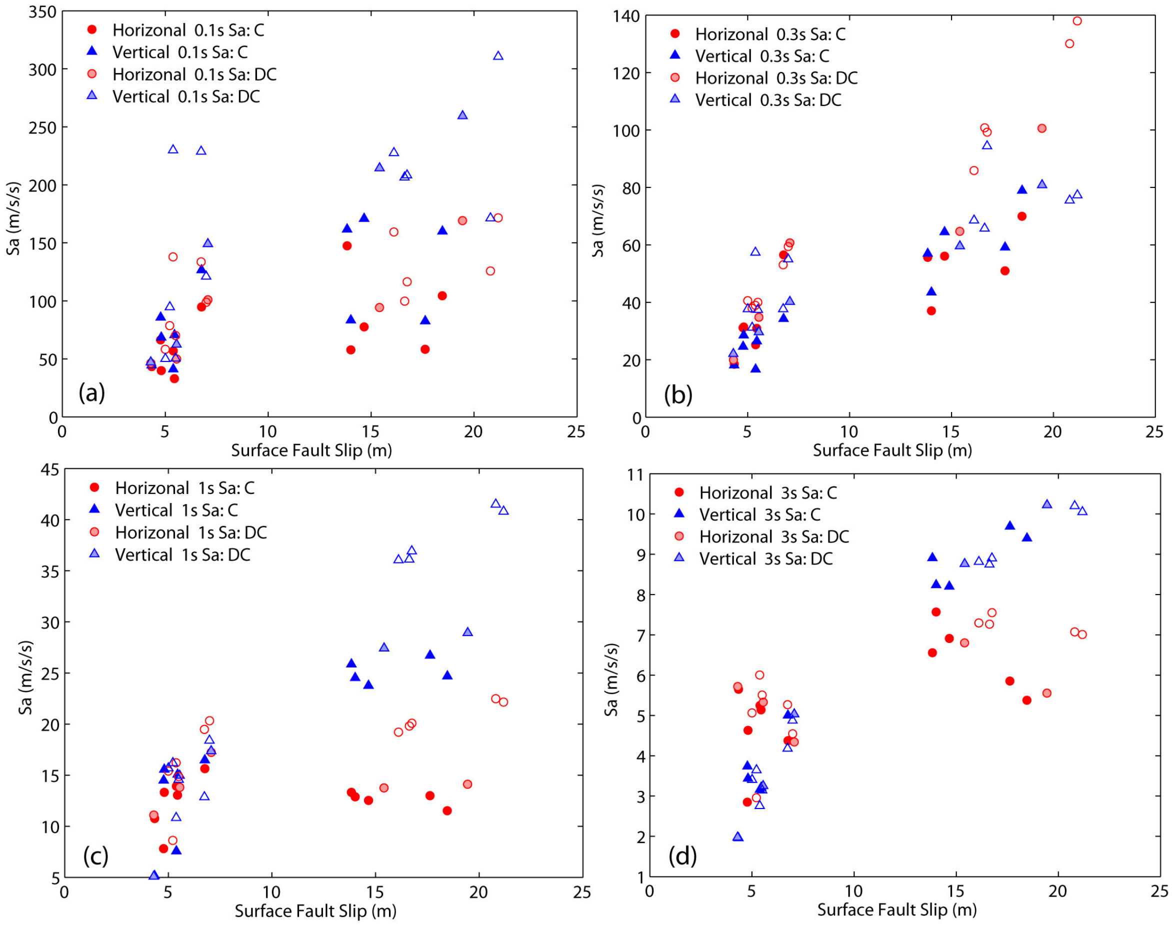
Horizonal 0.1s Sa: C
Vertical 0.1s Sa: C
Horizonal 0.1s Sa: DC
Vertical 0.1s Sa: DC
(a)
Sa (m/s/s)
Surface Fault Slip (m)
Horizonal 0.3s Sa: C
Vertical 0.3s Sa: C
Horizonal 0.3s Sa: DC
Vertical 0.3s Sa: DC
(b)
Sa (m/s/s)
Surface Fault Slip (m)
Horizonal 1s Sa: C
Vertical 1s Sa: C
Horizonal 1s Sa: DC
Vertical 1s Sa: DC
(c)
Sa (m/s/s)
Surface Fault Slip (m)
Horizonal 3s Sa: C
Vertical 3s Sa: C
Horizonal 3s Sa: DC
Vertical 3s Sa: DC
(d)
Sa (m/s/s)
Surface Fault Slip (m)

Figure 23